



Università degli Studi di Cagliari

Facoltà di Scienze Matematiche, Fisiche e Naturali

Laurea Magistrale in Fisica

**Observation-Guided Simulation of the
Extragalactic Binary Gravitational Wave
Foreground in View of LISA**

Relatore:

Prof. Riccardo Murgia

Co-relatori:

**Prof. Thomas Kupfer
Weitian Yu**

Candidato:

Gabriele Todde

Contents

Introduction	5
1 Theoretical Framework	7
1.1 Gravitational waves theory	7
1.1.1 Gravitational Waves as Perturbations	7
1.1.2 The physical wave	9
1.1.3 Motion and geodesics	10
1.1.4 The quadrupole approximation	12
1.1.5 Energy carried by a gravitational wave	15
1.1.6 Evolution of a compact binary system	16
1.2 White Dwarfs and Galaxies	18
1.2.1 White dwarfs	18
1.2.2 Galaxies	19
1.3 Gravitational Wave Interferometers	20
1.3.1 Michaelson interferometer	20
1.3.2 LISA	24
2 Methods and Data	27
2.1 Stellar Populations Synthesis Codes	27
2.1.1 The starting point	28
2.1.2 Single star evolution	28
2.1.3 Binary stars evolution	29
2.2 COSMIC	29
2.2.1 Fixed population	30
2.2.2 Astrophysical population	32
2.3 GWGC and Galaxy Properties	33
2.3.1 What it has vs what we need	33
2.3.2 Mass-luminosity relation	33
2.3.3 Mass-metallicity relation	34
2.3.4 Missing galaxies	35
2.4 Final Steps	38
2.4.1 The final fixed populations	39
2.4.2 LISA's frequency resolution	39
3 Results and Discussion	41
3.1 The Signal Computation	41

CONTENTS	4
Conclusions and Future Perspectives	45
A	47
B	49

Introduction

In the context of the gravitational waves study, there are mainly two possible paths: the first is the **analysis of existing data** from experiments like Ligo, Virgo and Kagra, with the goal of detecting and characterizing the observable sources within their relative frequency bands; the second is the **forecasting approach**, which aims to characterize future experiments in order to better understand what types of sources they could detect and how well.

One of the most important future detectors is the European *Laser Interferometer Space Antenna* (LISA), the first space-based gravitational wave detector. LISA will be arranged as an equilateral triangle with 2.5 million kilometers long arms, placed in a heliocentric orbit, and will operate within the frequency range from approximately 0.1mHz to 1Hz. Among the typical sources that emit gravitational wave signal in this range are the **compact binaries**, and in our particular case we are interested in **double white dwarf binaries** (WDBs).

The goal of this work is to estimate the gravitational wave background produced by the extragalactic WDBs in the local universe, by using the **COSMIC** code to generate synthetic astrophysical populations to represent the galaxies listed in the **Gravitational Wave Galaxy Catalog** (GWGC).

In **Theoretical Framework** we introduce the theoretical foundations of gravitational waves, derive the amplitude of the signal generated by a binary system, and define the most important parameters. We also give a broad theoretical astrophysical framework, briefly discussing the birth and evolution of double white dwarfs, both as single objects, and in binary systems, and the galactic environments that will host them. We then give a brief overview of how gravitational wave detectors work, trying to better understand what kinds of sources LISA will be able to see, what resolution and what sensitivity it will have and why in particular we are interested in WDBs.

In **Methods and Data** we introduce the concept of stellar population synthesis and the code COSMIC used for this purpose. We present its features, main parameters, and pipeline, and explain how it is used to generate full-size astrophysical populations of WDBs. In order to do this, we introduce the Gravitational Wave Galaxy Catalog, an observational survey that lists some of the key information we need for the purpose, and explain how we move from there to infer the remaining parameters. We then explain the procedure to generate the actual fixed populations, scale them to astrophysical full-size galaxies, and compute their gravitational wave signal. Moreover, we discuss how to take care of the lack of galaxies due to the catalog's incompleteness and the Milky Way coverage in the Zone Of Avoidance. Finally, we discuss the LISA frequency resolution

problem, and explain how we took it into account.

In **Results and Discussion** we present the results we found with the obtained information and the procedure we described, by plotting the total resulting signal on the LISA's sensitivity curve. We then discuss what we found, and the possible implications.

Finally, in the **Conclusions and Future Perspectives** we recap the work as a whole, discussing its limitations, assumptions and its possible extensions and follow-ups.

Chapter 1

Theoretical Framework

1.1 Gravitational waves theory

After considering, in 1905, the problem of the apparently *instantaneous* propagation of light, with the theory of Special Relativity, in 1916 Albert Einstein considered the problem of the apparently *instantaneous* propagation of gravity through *long distances*, in his theory of General Relativity. Einstein showed that long-distance interaction arises from the deformation of space time caused by massive objects. Hence, in the "static case", the deviated motion apparently caused by the interaction between two distant masses really is, in fact, a manifestation of space time curvature nearby, generated by the presence of the two objects. The "static case" just depicted, though, treats the curvature as if it had always been there, and doesn't take into account of any variation in the masses, positions or velocities of the two objects, that would induce an evolution to the curvature itself. In truth, after a change in the mass-energy distribution, the corresponding curvature variation requires its time to reach far distances, and a fascinating prediction of General Relativity is that it propagates in the form of a wave, that travels at the speed of light. For the treatment that follows, I have primarily relied on Ferrari et al. [2020], particularly Chapters 12, 13, and 14. I will not go into the full mathematical derivations here, but they are presented in detail in the book.

1.1.1 Gravitational Waves as Perturbations

The typical approach to the study of gravitational waves is to derive them as small perturbations of the background from the Einstein's equations:

$$G_{\mu\nu} = R_{\mu\nu} - \frac{1}{2}g_{\mu\nu}R, \quad (1.1)$$

which can be conveniently written as

$$R_{\mu\nu} = \frac{8\pi G}{c^4} \left(T_{\mu\nu} - \frac{1}{2}g_{\mu\nu}T \right), \quad (1.2)$$

where $G_{\mu\nu}$ is the Einstein tensor, $R_{\mu\nu}$ is the Ricci tensor, R is the Ricci scalar, $g_{\mu\nu}$ is the metric of space time, and $T_{\mu\nu}$ is the stress-energy tensor. As a background solution we can consider the flat space time described by the metric $\eta_{\mu\nu}$, to which the perturbation term

appears as a fluctuation in the metric $|h_{\mu\nu}| \ll |\eta_{\mu\nu}|$, known as *weak field* approximation. Thus, the perturbed space time can be written as:

$$g_{\mu\nu} = \eta_{\mu\nu} + h_{\mu\nu}, \quad |h_{\mu\nu}| \ll |\eta_{\mu\nu}|.$$

With this metric, the equations 1.2 becomes

$$\{\square_F h_{\mu\nu} - \left[\frac{\partial^2}{\partial x^\lambda \partial x^\mu} h_\nu^\lambda + \frac{\partial^2}{\partial x^\lambda \partial x^\nu} h_\mu^\lambda + \frac{\partial^2}{\partial x^\nu \partial x^\mu} h_\lambda^\lambda \right]\} = -\frac{16\pi G}{c^4} \left(T_{\mu\nu} - \frac{1}{2} \eta_{\mu\nu} T \right).$$

Now, by requiring that the *weak-field* approximation remains satisfied for infinitesimal diffeomorphisms, and by choosing a coordinate system in which the *harmonic gauge condition*¹, defined as

$$\Gamma^\lambda = g^{\mu\nu} \Gamma_{\mu\nu}^\lambda = 0, \quad (1.3)$$

where $\Gamma_{\mu\nu}^\lambda$ are the *affine connections*, is satisfied, we can find that, up to first order in $h_{\mu\nu}$, the harmonic gauge condition is equivalent to

$$\frac{\partial}{\partial x^\mu} h_\rho^\mu = \frac{1}{2} \frac{\partial}{\partial x^\rho} h, \quad h = \eta^{\mu\nu} h_{\mu\nu} \equiv h_\nu^\nu. \quad (1.4)$$

After defining the *trace-reversed*² tensor as

$$\bar{h}_{\mu\nu} \equiv h_{\mu\nu} - \frac{1}{2} \eta_{\mu\nu} h,$$

we can finally write the linearized Einstein equations as

$$\begin{cases} \square \bar{h}_{\mu\nu} = -\frac{16\pi G}{c^4} T_{\mu\nu}, \\ \partial^\mu \bar{h}_{\mu\nu} = 0. \end{cases}$$

This form, and its twin with $T_{\mu\nu} = 0$, where the first equation becomes the D'Alambert equation, are relevant because they show that *a perturbation of a flat space time propagates as a wave travelling at the speed of light*. As in Electrodynamics, the solution of (1.5) can be written in terms of *retarded potentials*:

$$\bar{h}_{\mu\nu}(t, \mathbf{x}) = \frac{4G}{c^4} \int_V \frac{T_{\mu\nu}(t - \frac{|\mathbf{x} - \mathbf{x}'|}{c}, \mathbf{x}')}{|\mathbf{x} - \mathbf{x}'|} d^3x', \quad (1.5)$$

where V is the three dimensional source volume, \mathbf{x}' is the distance of an element of the emitting source from the origin of a frame centered in the same point of the source, \mathbf{x} is the distance between source and observer. It can be proved that the solutions in (1.5) automatically satisfy the harmonic gauge condition in the second equation of the (1.5).

¹It is an arbitrary coordinate condition which makes it possible to solve the Einstein field equations. It can be found by requiring that the linearized Einstein equations satisfy the D'Alambert equation.

²The name comes by noting that $\bar{h} = \eta^{\mu\nu} \bar{h}_{\mu\nu} = -h$.

Harmonic gauge

It is important to notice that if the *harmonic gauge* condition is not satisfied in a reference frame, a new frame in which it is can always be found, by making an infinitesimal coordinate transformation

$$x^{\lambda'} = x^\lambda + \epsilon^\lambda, \quad (1.6)$$

provided that ϵ^λ satisfies the following equation:

$$\square_F \epsilon_\rho = \frac{\partial h_\rho^\beta}{\partial x^\beta} - \frac{1}{2} \frac{\partial h}{\partial x^\rho} = 0.$$

This is an inhomogeneous wave equation that can be solved to find the components ϵ_α , which identify the coordinate system in which the harmonic gauge condition is satisfied. Notice though, that the harmonic condition in (1.3) does not determine the gauge uniquely, but instead leaves some more gauge freedom to be used.

1.1.2 The physical wave

As we have seen, perturbations of flat space-time satisfy a wave equation and a harmonic gauge condition, as in (1.5). The general solutions of these wave equation is a linear superposition of monochromatic plane waves, with a polarization tensor (or wave amplitude) $A_{\mu\nu}$ and a wave four-vector \vec{k} , such as

$$\square_F \bar{h}_{\mu\nu} = -A_{\mu\nu} \eta^{\alpha\beta} k_\alpha k_\beta e^{ik_\gamma x^\gamma} = 0.$$

Thus, neglecting the trivial solution $A_{\mu\nu} = 0$, gives

$$\eta^{\alpha\beta} k_\alpha k_\beta = 0,$$

which means that \vec{k} is a null vector. If we also consider the harmonic gauge, we find a condition that imposes the orthogonality of the wave four-vector to the polarization tensor,

$$k_\mu A_\nu^\mu = 0.$$

The *wavefronts*, i.e. the spatial surfaces where $\bar{h}_{\mu\nu} = \text{const.}$ are the planes where $k_i x^i = \text{const.}$ Conventionally, k^0 is referred to as $\frac{\omega}{c}$, where ω is the frequency, thus

$$\vec{k}_0 = \left(\frac{\omega}{c}, \mathbf{k} \right),$$

where \mathbf{k} is the wave three-vector orthogonal to the wavefront, and is related to the *wavelength* by $|\mathbf{k}| = 2\pi/\lambda$. Notice that, since the wave four-vector \vec{k} is a null vector, it follows that

$$-(k^0)^2 + |\mathbf{k}|^2 = 0 \rightarrow \omega = ck_0 = c|\mathbf{k}|,$$

which gives the dispersion relation for a wave moving at the speed of light.

The TT gauge

In a one dimension case, the wave equation can be written as

$$\left(-\frac{1}{c^2} \frac{\partial^2}{\partial t^2} + \frac{\partial^2}{\partial x^2}\right) \bar{h}_\nu^\mu = 0,$$

which generally has, as solution, an arbitrary function of $t \pm \frac{x}{c}$. If we consider, for example, a progressive wave $\bar{h}_\nu^\mu[f(t, x)]$, where $f(t, x) = t - \frac{x}{c}$, and apply the harmonic gauge condition, focusing only in the time-dependent part of the solution, we find the *first four* conditions:

$$\bar{h}_t^t = \bar{h}_t^x, \quad \bar{h}_x^t = \bar{h}_x^x, \quad \bar{h}_y^t = \bar{h}_y^x, \quad \bar{h}_z^t = \bar{h}_z^x. \quad (1.7)$$

As we have already discussed, there still is the freedom of making an infinitesimal coordinate change, and by requiring that the harmonic gauge remains satisfied in the new coordinates generates *four more conditions*:

$$\bar{h}_x^t = \bar{h}_y^t = \bar{h}_z^t = \bar{h}_y^x + \bar{h}_z^x = 0, \quad (1.8)$$

and with the (1.7) follows

$$\bar{h}_x^x = \bar{h}_y^x = \bar{h}_z^x = \bar{h}_t^x = 0.$$

The only non zero components are \bar{h}_y^z and $\bar{h}_y^y - \bar{h}_z^z$, which cannot be set to zero because now we have completely used all the gauge freedom. It can be shown that, from all the above conditions, it follows that $\bar{h} \equiv h$, i.e. in this gauge the wave results to be *traceless*. Thus, a plane gravitational wave propagating along the x -axis is characterized by only two non-zero functions h_{zy} and $h_{yy} = -h_{zz}$:

$$h_{\mu\nu}^{TT} = \begin{pmatrix} 0 & 0 & 0 & 0 \\ 0 & 0 & 0 & 0 \\ 0 & 0 & h_{yy} & h_{yz} \\ 0 & 0 & h_{yz} & -h_{yy} \end{pmatrix}. \quad (1.9)$$

In conclusion, the gravitational wave only has **two physical degrees of freedom** which correspond to two polarization states. This gauge is called **TT gauge** because of the *transverse traceless* nature: $h_{\mu\nu}$ is traceless, thus $h = 0$, and transverse, since the components of $h_{\mu\nu}$ along the direction of propagation are null (in this case $h_{\mu x} = 0$).

1.1.3 Motion and geodesics

Free test particles in General Relativity move along geodesic, which means that, in terms of a world line $x^\mu(\tau)$ parametrized by proper time τ , they satisfy the *geodesic equation*:

$$\frac{d^2 x^\alpha}{d\tau^2} + \Gamma_{\mu\nu}^\alpha \frac{dx^\mu}{d\tau} \frac{dx^\nu}{d\tau} \equiv \frac{du^\alpha}{d\tau} + \Gamma_{\mu\nu}^\alpha u^\mu u^\nu = 0, \quad (1.10)$$

where $u^\alpha = \frac{dx^\alpha}{d\tau}$ is the particle velocity. By imposing the rest condition, $u^\alpha = (1, 0, 0, 0)$, to the (1.10) and considering the TT gauge component prescriptions for $h_{\mu\nu}$, we find that a particle initially at rest is not accelerated by the passage of a wave, but remains at a fixed coordinate position: the motion of a single particle is not affected by the gravitational waves.

The geodesic deviation

If we consider, instead, the relative motion of close particles, the situation is different. This relative motion is governed by the *geodesic deviation*, which quantifies how two very close geodesics deviate from one another. Although, as we have seen, the coordinates of the two particles (and thus their difference) do not change when a gravitational wave passes, this does not hold true for their *proper distance* Δl

$$\Delta l = \int ds \neq \text{const.}$$

This apparent contradiction arises from the fact that the coordinate difference is not a *tensorial* quantity, and therefore is not suited to describe properly a physical process. This is the reason we consider the geodesic deviation, which provides a tensorial formulation of the relative acceleration between the two particles:

$$\frac{D^2 \delta x^\alpha}{d\tau^2} \equiv (\Delta_{\vec{t}}(\Delta_{\vec{t}} \vec{\delta x}))^\alpha = R^\alpha_{\beta\mu\nu} t^\beta t^\mu \delta x^\nu, \quad (1.11)$$

where

$$R_{\alpha k \lambda \mu} = \frac{1}{2}(g_{\alpha\mu, \lambda k} + g_{k\lambda, \mu\alpha} - g_{\alpha\lambda, \mu k} - g_{k\mu, \lambda\alpha}) \quad (1.12)$$

is the Riemann curvature tensor, \vec{t} is the tangent vector to one of the geodesic, and $\vec{\delta x}$ is a deviation vector between the two geodesics. It is important to note that in the presence of a gravitational wave the Riemann tensor is never zero in any reference frame, and consequently neither is the geodesic deviation. In contrast, the quantity $\frac{d^2 \delta x^i}{d\tau^2}$ (which is not a tensorial quantity) vanishes in the TT frame.

Knowing this, to analyze this effect in more detail we can choose to integrate the (1.11) in a *Locally Inertial Frame*, LIF $\{\xi^\alpha\}$, centered on one of the two particles, where the metric can be approximated close to the origin as Minkowski up to quadratic, negligible, corrections:

$$ds^2 = \eta_{\alpha\beta} d\xi^\alpha d\xi^\beta + O(|\xi|^2).$$

In this frame, the Riemann tensor in (1.12), which depends on second derivatives of the metric perturbation $h_{\mu\nu}$ (with $g_{\mu\nu} = \eta_{\mu\nu} + h_{\mu\nu}$), is not only covariant, but actually *invariant* under infinitesimal coordinate transformations from a generic LIF to the TT frame. This is especially useful because in the TT frame $h_{\mu\nu}^{TT}$ takes a particularly simple form, as we have seen in the (1.9) example, simplifying also the expression for $R_{\alpha k \lambda \mu}^{TT}$. Assuming that the wave travels along the ξ^1 direction, the solutions for the geodesic deviation equation for two close particles are the non zero components of

$$\delta \xi_0^j = \delta \xi_0^j + \frac{1}{2} \eta^{ji} h_{ik}^{TT} \delta \xi_0^k, \quad (1.13)$$

where $\delta \xi_0^j$ represent the initial, constant separation between the particles. As previously discussed, the non-zero components of the strain tensor h_{ik}^{TT} correspond to two possible polarizations of the gravitational wave. Their distinct effects on a ring of close particles are visually represented in **Figure 1.1**.

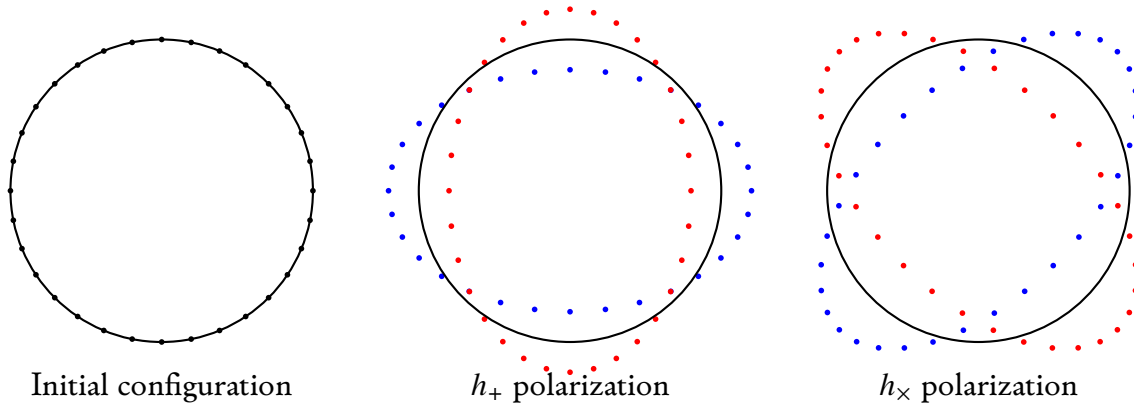


Figure 1.1: Effect of the two gravitational wave polarizations on a ring of free-falling particles, caused by a wave moving in the direction perpendicular to the page: blue and red dots represent two opposite phases of the wave.

1.1.4 The quadrupole approximation

Now that we have discussed the effects of the passage of a gravitational wave on the relative motion of close particles, we can focus on another important problem: *how such waves are generated*. Gravitational radiation is a consequence of variations in the spacetime curvature, and it generates from time-dependent distributions of mass and momentum. But not every motion of matter can produce gravitational wave signal, as we will see: conservation laws of general relativity, impose strict constraints on the possible multipole moment that can contribute to the tensorial metric perturbations.

The weak-field, slow-motion approximation

We already introduced previously the weak-field limit, which allows us to write the metric as a perturbed Minkowski $g_{\mu\nu} = \eta_{\mu\nu} + h_{\mu\nu}$, with $|h_{\mu\nu}| \ll 1$, and we found the solutions as in (1.5). Until now, we have only solved these equations with a null stress-energy tensor. If we assume that the region, of size ϵ , where the source of the signal is confined, is much smaller than the wavelength of the emitted gravitational radiation, $\lambda_{GW} = \frac{2\pi c}{\omega}$, we find the following condition:

$$\frac{2\pi c}{\omega} \gg \epsilon \rightarrow \epsilon\omega \ll c \rightarrow v_{\text{typical}} \ll c. \quad (1.14)$$

The typical velocities of the system are much smaller than the speed of light: this is the so called *slow motion approximation*. If we now use the solution found using the retarded potentials in (1.5), by making use of the Fourier transforms it can be found that the gravitational wave signal emitted by the source, to leading order in the weak-field, slow-motion approximation is

$$\bar{h}_{\mu\nu}(t, r) = \frac{4G}{rc^4} \int_V T_{\mu\nu}(t - \frac{r}{c}, \mathbf{x}') d^3x. \quad (1.15)$$

The quadrupole formula

The integral in (1.15) can be simplified with some expedients. First of all, by making use of the conservation law that applies to the stress-energy tensor

$$\frac{\partial T^{\mu\nu}}{\partial x^\nu} = 0, \quad \rightarrow \quad \frac{1}{c} \frac{\partial T^{\mu 0}}{\partial t} = -\frac{\partial T^{\mu k}}{\partial x^k}, \quad \mu = 0, \dots, 3, \quad k = 1, 2, 3,$$

a smart use of the Gauss' theorem (reminding that the stress-energy tensor is null on the source's surface), it can be found that

$$\bar{h}^{\mu\nu} = 0.$$

Secondly, we can use the **tensor-virial theorem**

$$\frac{1}{c^2} \frac{\partial^2}{\partial t^2} \int_V T^{00} x^k x^n d^3x = 2 \int_V T^{kn} d^3x, \quad k, n = 1, 2, 3, \quad (1.16)$$

in the definition of the **quadrupole moment tensor**

$$q^{kn}(t) = \frac{1}{c^2} \int_V T^{00}(t, \mathbf{x}) x^k x^n d^3x, \quad (1.17)$$

we finally find that (1.15) can be re-written as

$$\begin{aligned} \bar{h}^{\mu 0} &= 0, \\ \bar{h}^{ik}(t, r) &= \frac{2G}{c^4 r} \frac{d^2}{dt^2} q^{ik}\left(t - \frac{r}{c}\right), \end{aligned} \quad (1.18)$$

known as the **quadrupole formula**. This formulation describes the gravitational wave signal emitted by a gravitating system that evolves in time, whatever the mass-energy distribution looks like, as long as $\ddot{q}^{ik} \neq 0$. Note that in this approximation, the only component of the stress-energy tensor that generates the metric perturbation is T^{00} , and that the c^{-4} renders the characteristic strain extremely small:

$$\frac{G}{c^4} \sim 10^{-49} \frac{s^2}{g \text{ cm}}.$$

Transform to the TT gauge

The solution in (1.18) represents a spherical wave far from the source, which locally looks like a plane wave. It can also be expressed, after an infinitesimal coordinate transformation that preserves the harmonic gauge. This projection in the TT gauge is performed by defining symmetric and transverse *projector operators* as

$$P_{jk} \equiv \delta_{jk} - n_j n_k,$$

to then define the **transverse-traceless projector**

$$P_{jkmn} \equiv P_{jm} P_{kn} - \frac{1}{2} P_{jk} P_{mn}, \quad (1.19)$$

which "extracts" the transverse-traceless part of a rank two tensor on the three-dimensional Euclidean space. This way we can, for example, define

$$h_{jk}^{TT} = P_{jkmn} \bar{h}_{mn},$$

that, if applied to the (1.18), gives

$$\begin{aligned} \bar{h}_{\mu 0}^{TT} &= 0, \\ \bar{h}_{ik}^{TT}(t, r) &= \frac{2G}{c^4 r} \frac{d^2}{dt^2} Q_{ik}^{TT} \left(t - \frac{r}{c}\right), \end{aligned} \quad (1.20)$$

where $Q_{jk}^{TT} = P_{jkmn} q_{mn}$ is the transverse-traceless part of the quadrupole moment. As we will see, to compute the "luminosity" of a gravitational wave source, it is useful to define the **reduced quadrupole moment**

$$Q_{jk} \equiv q_{jk} - \frac{1}{3} \delta_{jk} q_m^m, \quad (1.21)$$

which is traceless by definition.

Gravitational waves from a binary system

As an example, we can consider a binary system where two masses m_1 and m_2 are in a circular orbit around the common center of mass. The typical parameters are the total mass

$$M \equiv m_1 + m_2,$$

the *reduced mass*

$$\mu \equiv \frac{m_1 m_2}{M},$$

and, by placing the origin of the coordinate frame in the center of mass,

$$l_0 = r_1 + r_2, \quad r_1 = \frac{m_2}{M} l_0, \quad r_2 = \frac{m_1}{M} l_0, \quad \omega_K = \sqrt{\frac{GM}{l_0^3}}.$$

Now, after defining the coordinates of the masses (x_1, y_1) and (x_2, y_2) in an orbital plane, orthogonal to the z -axis, as functions of all the above parameters, it becomes possible to compute the 00-component of the stress-energy tensor as

$$T^{00} = c^2 \sum_{n=1}^2 m_n \delta(x - x_n) \delta(y - y_n) \delta(z),$$

and thus all the non-vanishing components of q_{jk} . From this we can find Q_{jk} , Q_{jk}^{TT} , and finally

$$h_{ij}^{TT}(t, r) = -\frac{A}{r} A_{ij}^{TT} \left(t - \frac{r}{c}\right), \quad (1.22)$$

where³

$$\begin{aligned} A &= \frac{4\mu MG^2}{l_0 c^4}, \\ A_{ij}^{TT}(t - \frac{r}{c}) &= P_{ijkl} A_{kl}(t - \frac{r}{c}), \\ A_{kl}(t) &= \begin{pmatrix} \cos 2\omega_K t & \sin 2\omega_K t & 0 \\ \sin 2\omega_K t & -\cos 2\omega_K t & 0 \\ 0 & 0 & 0 \end{pmatrix}. \end{aligned} \quad (1.23)$$

Using typical values, such as the PSR 1913+16 assuming it had a circular orbit, by defining

$$h_0 = \frac{A}{r},$$

and using (1.23), we find

$$h_0 \sim 5 \times 10^{-23}, \quad (1.24)$$

as an estimate of a typical gravitational wave signal amplitude generated by a binary system.

1.1.5 Energy carried by a gravitational wave

The stress-energy tensor conservation laws that we know in Special relativity

$$T_{,\nu}^{\mu\nu} = 0,$$

unfortunately do not hold in General Relativity. Indeed, the Stress-energy tensor describes the energy and momentum of the sources of the gravitational field, but not of the gravitational field itself: to have a proper conservation we would need to consider both contributions. The equivalence principle states that the effect of the gravitational field vanishes in a LIF centered on a particle; if there was a tensor describing it, it would be null in this frame too. But if a tensor field is null in one frame, than it must be in all the other too: for this reason, there cannot be anything like a true gravitational field tensor.

Stress-energy pseudo-tensor

For this reason, we are going to introduce a **stress-energy pseudo tensor**, where a pseudo-tensor is a mathematical object that behaves like a tensor only under linear coordinate transformations. It is possible to define procedures of *integration* or *averaging* involving it, which allow to construct well-defined gauge-invariant quantities. In particular, it is possible to define a *local* notion of energy and momentum in the weak field approximation, on the assumption that the characteristic length-scale λ of the perturbation is much smaller than the characteristic length-scale L of the background: $\lambda/K \ll 1$. In this regime, it can be shown that if averaged over multiple wavelengths λ , the stress-energy pseudo-tensor transforms as a tensor for coordinate transformations linear in h (i.e. of order $O(h)$),

$$\langle t^{\mu\nu} \rangle,$$

and is therefore *suitable to describe energy and momentum carried by the perturbation*.

³Note that this shows that a *binary system in circular orbits emits waves at twice the orbital frequency*

Gravitational wave luminosity

In general, it can be shown that the energy flowing across a unit surface orthogonal to the direction x' per unit time is given by the $0x'$ component of the stress-energy tensor times the speed of light. Similarly, the energy flux of a gravitational wave propagating in the same direction is given by the same component of the stress-energy pseudo-tensor averaged over several wavelengths, and can be derived as

$$\frac{dE_{GW}}{dt dS} = c \langle t^{0x'} \rangle = \frac{c^3}{16\pi G} \langle (\dot{h}_+(t, x'))^2 + (\dot{h}_x(t, x'))^2 \rangle.$$

where h_+ and h_x are the analog of h_{yy} and h_{yz} in the (1.9), and represent the metric perturbation polarizations. In the TT frame, by directly substituting what we have found in (1.20), we find

$$\frac{dE_{GW}}{dt dS} = \frac{G}{8\pi c^5 r^2} \left\langle \sum_{jk} \left(\ddot{Q}_{jk}^{TT} \left(t - \frac{r}{c} \right) \right)^2 \right\rangle,$$

and after defining the **gravitational wave luminosity** as

$$L_{GW} = \frac{dE_{GW}}{dt} = \int \frac{dE_{GW}}{dt dS} dS,$$

and writing Q^{TT} as a function of (1.21), by using the TT projectors in (1.19) and their properties, it can be shown that the energy associated to a gravitational wave can be written as the **luminosity quadrupole formula**:

$$L_{GW}(t) = \frac{G}{5c^5} \left\langle \left(\ddot{Q}_{ij} \left(t - \frac{r}{c} \right) \right) \left(\ddot{Q}_{ij} \left(t - \frac{r}{c} \right) \right) \right\rangle, \quad (1.25)$$

as was derived by Einstein in Einstein [1918].

1.1.6 Evolution of a compact binary system

By applying what we have found in the previous subsection to real astrophysical sources of gravitational wave, in this section we will find the amplitude that we are going to use for this thesis work to generate the total gravitational wave signal. In particular, we can apply the general results we found for two objects in a circular orbit in (1.23) to compute the quadratic sum of the components of \ddot{Q}_{ij} in (1.25), and find the gravitational wave luminosity of a compact binary system as

$$L_{GW} = \frac{32}{5} \frac{G^4}{c^5} \frac{\mu^2 M^3}{l_0^5}$$

Remember that this represents an average over several wavelengths, and thus, of course, over many orbital periods (since $\omega_{GW} = \omega_K$), which makes it applicable only for systems that do not change significantly over a large number of periods (very far from merger), an assumption that is called *adiabatic approximation*. The energy emitted in gravitational waves comes from the total energy of the system, which is in part kinetic and in part potential energy. By requiring the time derivative of the two to be equal, we can find

how the binary parameters must change accordingly. For example, the distance between the two objects shortens with time as

$$l_0(t) = l_0^{in} \left(1 - \frac{t}{t_c}\right)^{1/4}, \quad \text{where} \quad t_c \equiv \frac{5}{256} \frac{c^5}{G^3} \frac{(l_0^{in})^4}{\mu M^2}. \quad (1.26)$$

Using Kepler's laws it is also possible to translate this in a time dependence on the frequency:

$$\omega_K(t) = \omega_K^{in} \left(1 - \frac{t}{t_c}\right)^{-3/8}, \quad \text{where} \quad \omega_K^{in} \equiv \frac{(GM)^{1/2}}{(l_0^{in})^{3/2}}. \quad (1.27)$$

or the period

$$P(t) = P^{in} \left(1 - \frac{t}{t_c}\right)^{3/8}. \quad (1.28)$$

Signal from inspiralling compact objects

Now that we have seen how the orbital parameters should change we can finally find the gravitational wave signal for an *inspiralling compact object*. We have already found in (1.22) the general strain solution for a binary system, where its useful to redefine the instantaneous amplitude as

$$h_0 = \frac{A}{r} = \frac{4\mu MG^2}{l_0 c^4 r},$$

where r is the distance from the source, and l_0 the distance between the two objects. Moreover, l_0 can be written in terms of the angular frequency, using Kepler's law and (1.27), to get

$$h_0(t) = \frac{4\pi^{2/3} G^{5/3} M_{ch}^{5/3}}{r c^4} v_{GW}^{2/3}(t),$$

where

$$M_{ch} = \mu^{3/5} M^{2/5} = \frac{(m_1 m_2)^{3/5}}{M^{1/5}}, \quad (1.29)$$

is the **chirp mass**, and

$$v_{GW}(t) = \frac{v_{GW}^{in} t_c^{3/8}}{(t_c - t)^{3/8}}, \quad (1.30)$$

is the gravitational wave frequency. By substituting t_c as defined in (1.26), we finally find the signal emitted during the inspiral as

$$h_{ij}^{TT}(t, r) = -h_0 \left(t - \frac{r}{c}\right) P_{ijkl} A_{kl} \left(t - \frac{r}{c}\right), \quad (1.31)$$

where

$$h_0(t) = \frac{4\pi^{2/3} G^{5/3}}{c^4} \frac{M_{ch}}{r} (M_{ch} v_{GW}(t))^{2/3} \quad (1.32)$$

is the wave amplitude that we are going to refer to in this thesis work, when we calculate the signal from the simulated binaries⁴.

⁴ANYTHING ABOUT COSMOLOGICAL CORRECTIONS?

1.2 White Dwarfs and Galaxies

In this section, we will introduce the main astrophysical theory elements for the gravitational wave sources we want to simulate. First of all, we focus on white dwarfs, the compact remnants of low- and intermediate-mass stars, both as isolated objects or as components of binary systems. We then shift our discussion to galaxies, the large-scale environments in which these compact binaries form and evolve. The properties of galaxies, including their morphology, stellar populations, and dynamical structure, strongly influence the formation rates, spatial distribution, and evolution of white dwarf binaries. A clear understanding of both the compact objects themselves and their host galaxies is necessary for predicting the gravitational wave signals that can be observed.

1.2.1 White dwarfs

During its evolution, a star generates energy in its core through the nuclear fusion reactions, "burning" the elements in its core. During this process, which represents most of the star's life, the *radiation pressure* generated holds the star from the gravitational collapse. For most stars, this process begins with the fusion of hydrogen into helium, and when the core runs out of hydrogen, it contracts while the external layers expand: the luminosity is now spread in a larger surface, and since the *black body energy density* is $\propto T^4$, where T is the surface temperature, the star will look colder and larger, as a *red giant*. If the star is sufficiently massive, core contraction raises the temperature enough to ignite helium fusion into heavier elements, leading to subsequent burning stages. In contrast, for medium or low massive stars ($M_* \leq 8M_\odot$), after the red giant phase the central pressure is initially insufficient to ignite heavier fusion, and the contraction continues until the *electron degeneracy pressure* (a quantum mechanical effect arising from the Pauli exclusion principle) halts it. In such stars, when the helium starts burning the emitted radiation is not sufficient to push back against the enormous gravitational pressure. At this point a runaway process can be initialized, in which the core keeps compressing, and heating, and the fusion rate increases. This positive feedback process induces a very fast helium burning called *helium flash*, that lifts the star back out of the degeneracy stage. The cycle of contraction and fusion continues until the core is composed of an element that cannot be fused under the prevailing conditions — either because the temperatures are too low, or because the reactions would no longer be exothermic (as in the case of iron). Moreover, for low and intermediate-mass stars, intense winds and envelope ejections during late stages of the evolution can strip away the outer layers, leaving behind a naked, degenerate core. These types of medium-to-low massive star's remnant, supported entirely by electron degeneracy pressure and slowly cooling over time, is what we call a **white dwarf**.

Binary systems

A great fraction of the white dwarfs in the universe are found in binary systems, known as **double white dwarfs (DWDs)**, that show a wide range of orbital separations and periods, depending on their formation and evolutionary history. In particular, in the Milky Way, DWDs are expected to be extremely common systems, many of which having orbital periods short enough to emit gravitational waves in the milliHertz band.

Between the most relevant parameters for DWDs, with a particular focus for those that affect the gravitational wave signal in (1.32), typical values are:

- **Masses:** typically between $0.2 M_{\odot}$ and $1.2 M_{\odot}$, with the most common systems having total masses $M_{\text{tot}} \sim 0.6\text{--}1.0 M_{\odot}$.
- **Radii:** $\sim 0.01 R_{\odot}$ ($\approx 7 \times 10^3$ km), decreasing with increasing mass according to the mass–radius relation for degenerate matter.
- **Orbital periods:** between $\sim 10^4$ s (a few hours) and $\lesssim 300$ s (5 minutes) for the most compact systems.
- **Gravitational wave frequencies:** $f_{\text{GW}} = 2/P_{\text{orb}}$, hence in the range $\sim 0.1\text{--}10$ mHz for LISA-relevant binaries.

In some binaries, the DWDs are detached, and neither star fills its Roche lobe, while in interacting systems there might be mass transfers. In these cases, once one of the white dwarfs overflows its own Roche lobe, material flows through the inner Lagrangian point toward the companion. The nature of this transfer depends on the mass ratio: the transfer can be stable, leading to long-lived systems characterized by persistent mass accretion and bright electromagnetic counterparts, or it can become dynamically unstable, potentially resulting in the rapid merger of the two stars, which may produce a single more massive white dwarf, a neutron star, or even trigger a thermonuclear explosion if the critical conditions for a Type Ia supernova are met.

1.2.2 Galaxies

Galaxies are the fundamental building blocks of the large-scale structure of the Universe. They host the vast majority of stars, stellar remnants, and interstellar matter, and therefore also the majority of DWDs, and represent the environment in which such objects are generated and evolve. At the same time, their distribution in space and their physical properties affect the detectability of the gravitational-wave signals produced by these binaries.

Morphological types

Their role as environment in which DWDs are born and evolve, their properties are fundamental because they influence it greatly. It becomes thus necessary to categorize them, in order to schematize the most important differences in this perspective. The classical way to classify them is based on their morphology, as first organized by Hubble [1926] into the *Hubble sequence*. This classification broadly distinguishes between:

- **Elliptical galaxies (E):** They present smooth, featureless light profiles with nearly elliptical shape, and they are mostly populated by older stars and very little interstellar medium, and show little to no ongoing star formation. They range from nearly spherical (E0) to highly elongated ellipses (E7), depending on the eccentricity.
- **Lenticular galaxies (S0):** An intermediate class between elliptical and spiral galaxies, they present a central bulge and a disk but do not have prominent spiral arms. They also often contain older stars and have low gas content, but their flattened structure suggests a disk-like stellar kinematics.

- **Spiral galaxies (Sa, Sb, Sc, Sd):** Like our own, they are disk galaxies with spiral arms rooted in a central bulge. Early-type spirals (Sa) have tightly wound arms and larger bulges, whereas late-type spirals (Sc, Sd) have more open arms, smaller bulges, and more gas and young stars.
- **Irregular galaxies (Irr):** They lack of a defined shape, and are often rich in gas and undergoing intense star formation, possibly as a result of interactions or mergers.

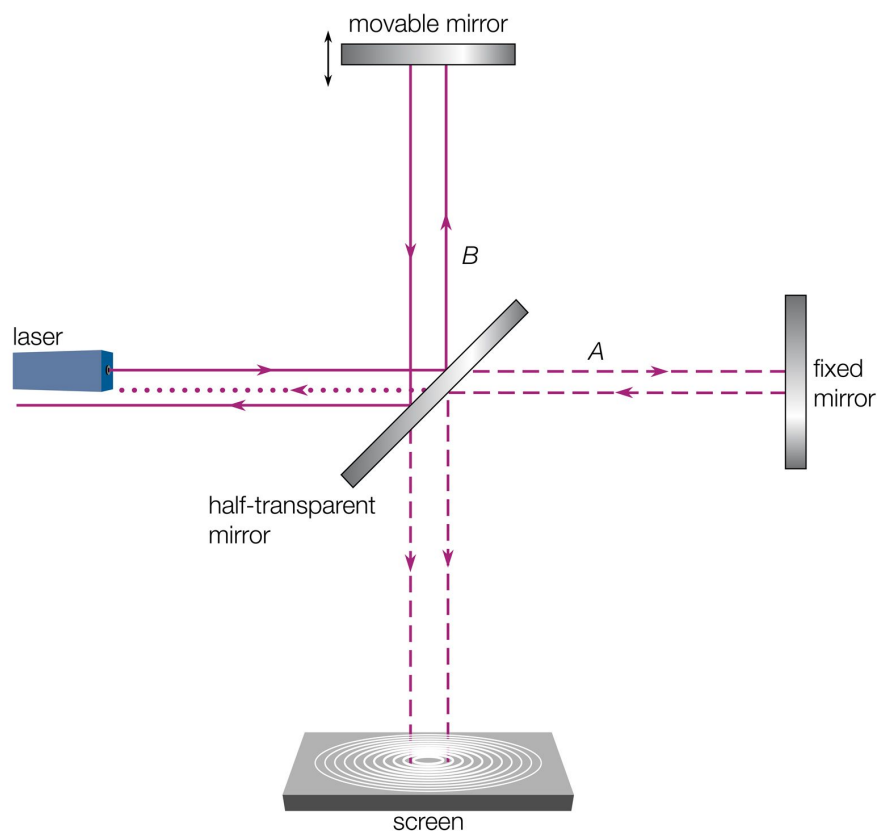
For quantitative studies as the present one, morphological types can be conveniently parameterized by the **T-value** introduced in the *Third Reference Catalogue of Bright Galaxies* (de Vaucouleurs et al. 1991), which allows an easy mapping between the numerical index and the traditional Hubble sequence morphology. This system assigns values from $T = -6$ (E ellipticals) through $T \approx 0$ (S lenticulars), to $T \approx 10$ (irregulars), with intermediate integers corresponding to specific spiral subclasses (Sa, Sb, Sc, etc.). Note that the difference in the age of the stars populating the different morphological types illustrated translates in a systematic variation in the typical metallicity values, with early types generally being more metal-rich on average than late types. This metallicity fingerprint that distinguishes morphological types will be an important feature in the next chapters, where the stellar population properties will influence the compact binary formation and gravitational wave emission.

1.3 Gravitational Wave Interferometers

As we have shown in (1.24), the typical gravitational wave amplitude for a binary system is very small, and this makes it quite a hard task to detect it. The most sensitive instrument that are capable of such measurements are the interferometric detectors, that are generally based on the same principle of the simple Michaelson interferometer: by splitting a laser beam along two perpendicular arms and recombining it, they detect the small phase shifts induced by a passing gravitational wave. In this section, which is mainly based on the chapter 9 of Maggiore [2007], we explain the general working principle of interferometers using the Michaelson interferometer as an example. After this, we will talk briefly about LISA's characteristics, and what makes it interesting for future research.

1.3.1 Michaelson interferometer

The Michaelson interferometer is an optical instrument invented in 1887 in occasion of the Michaelson-Morley experiment, with the purpose of measuring changes in the travel time of light due to its relative motion with respect to *ether*. It uses a *beam splitter* to separate a single laser beam into two independent, and perpendicular paths, that end up recombining via the superposition principle before meeting the photoelectric detector or camera, as represented in Figure 1.2. The laser is used to have a monochromatic light source, with a frequency ω_L , a wave-vector $k_L = \omega_L/c$ and a wavelength $\lambda_L = 2\pi/k_L$. Therefore, referring to Figure 1.2, we label as A and B respectively the x and y arms of the interferometer, with lengths L_A and L_B . If t_0 is the time the beam reaches the beam splitter the first time, it will come back to it from the two paths at time $t = t_0 + 2L_A/c$ and $t' = t_0 + 2L_B/c$. The detector only sees one single recombined beam, not two beams



© 2010 Encyclopædia Britannica, Inc.

Figure 1.2: Schematic representation of a Michelson interferometer. A laser beam is split by a half-transparent mirror into two orthogonal arms of length L_A and L_B . The beams reflected from the mirrors are recombined at the detector (screen), where, if a gravitational wave has passed, they produce an interference pattern. Variations in the optical path length of one arm (through the movable mirror) shift the observed fringes. The source for this image is at <https://www.britannica.com/technology/Michelson-interferometer>.

arriving at different times, so in its perspective, if one had to cross a longer distance than the other it had to have started its journey before the other, meaning $t \equiv t'$, and the two beams start at $t_0^{(A)} = t - 2L_A/c$ and $t_0^{(B)} = t - 2L_B/c$. If we set the beam splitter at the origin of the frame, this initial time difference translates in a phase difference between the two separate beams. If the phase is conserved during the free propagation, there are some factors acquired by the field during the reflections and refractions, and the overall effect gives the two electric fields that will recombine at the beam splitter as

$$\begin{cases} E_1 = -\frac{1}{2}E_0 e^{-i\omega_L t + 2ik_L L_A} \\ E_2 = -\frac{1}{2}E_0 e^{-i\omega_L t + 2ik_L L_B}, \end{cases} \quad (1.33)$$

The total electric field is the sum of the two, and after some re-writing it can be shown that the power measured by the photodetector is

$$|E_{out}|^2 = E_0^2 \sin^2[k_L(L_A - L_B)], \quad (1.34)$$

therefore any variation in the lengths of the two arms corresponds to a variation in the power measured at the photodetector. Note that, since $k_L = 2\pi/\lambda_L$, the (1.34) becomes

$$|E_{out}|^2 = \frac{1}{2}E_0^2 \left[1 - \cos\left(\frac{4\pi}{\lambda_L}\Delta L\right) \right],$$

therefore the detector measures a value depending on the cosine, which in turn depends on ΔL : if there is no gravitational wave, I would expect a null measure.

Gravitational waves and TT gauge

The TT gauge describes the position of *free falling* objects, that does not change when a gravitational wave passes. In order to replicate this condition the mirrors of the interferometers should also be "free falling", but instead their fall is halted by suspensions. This apparent problem is solved when considering that the effects of gravitational waves are perpendicular to their direction of motion, and therefore the mirrors need to be decoupled in the horizontal plane, rather than the vertical. For this reason, the mirrors are suspended, and as far as the motion in the horizontal plane is concerned they can be taken to be following the geodesics of the time-dependent part of the gravitational field. Thus, in the TT gauge the coordinates of the beam splitter (at the origin) and of the mirrors - at $(L_A, 0)$ and $(0, L_B)$ - are not affected by the passage of a wave, but the propagation of light in the arms is. Assuming a *plus-polarized* gravitational wave moving in the z direction, perpendicular to the plane defined by the two arms, we have

$$h_+(t) = h_0 \cos \omega_{gw} t,$$

and the space-time interval in the TT frame will be given by

$$ds^2 = -c^2 dt^2 + [1 + h_+(t)]dx^2 + [1 - h_+(t)]dy^2 + dz^2.$$

Since photons follow the null geodesic, we can set $ds = 0$, and, considering the arm in the x direction as an example, we get

$$dx = \pm c dt \left[1 - \frac{1}{2}h_+(t) \right],$$

where the sign depends on the direction of motion with respect to the origin. These can be used to write the length of the arms as the time integral from the beam splitter at t_0 , to the mirror at time t_1 , or from this time back to the beam splitter, at t_2 , in order to find the total time interval in which the light has traveled along the arms. By neglecting terms $O(h^2)$, and using some trigonometric identities, we can find the time interval for the x -axis arm as

$$t_2 - t_0 = \frac{2L_A}{c} + \frac{L_A}{c} h(t_0 + L_A/c) \frac{\sin(\omega_{gw} L_A/c)}{(\omega_{gw} L_A/c)}, \quad (1.35)$$

where

$$\text{sinc}\left(\frac{\omega_{gw} L}{c}\right) \equiv \frac{\sin(\omega_{gw} L/c)}{(\omega_{gw} L/c)} \xrightarrow{\frac{\omega_{gw} L}{c} \rightarrow 0} 1.$$

Therefore, when the period of the gravitational wave is large with respect to the time it takes the light to travel along the arm, the Δt shift in the travel time $t_2 - t_0$, with respect to the unperturbed case is simply $h(t_1)L_A/c$. In the opposite case, when $\omega_{gw} L_A/c \gg 1$, $h(t)$ will change sign many times during the travel time, making its net contribute ~ 0 . Now, from (1.35) and its y -axis counterpart, it is possible to find the two different starting time we have talked about, $t_0^{(x)}$ and $t_0^{(y)}$ ⁵. By substituting them in the electric field expressions in (1.33) we can find

$$\begin{cases} E^{(x/y)} = \mp \frac{1}{2} E_0 e^{-i\omega_L t_0^{(x/y)}} \\ \quad = \mp \frac{1}{2} E_0 e^{-i\omega_L \left(t - \frac{L_{A/B}}{c}\right) + i\Delta\phi_{x/y}(t)}, \end{cases} \quad (1.36)$$

where

$$\Delta\phi_{x/y} = \pm h_0 \frac{\omega_L L_{A/B}}{c} \text{sinc}\left(\omega_{gw} \frac{L_{A/B}}{c}\right) \cos\left[\omega_{gw} \left(t - \frac{L_{A/B}}{c}\right)\right], \quad (1.37)$$

is the phase difference from the unperturbed case in the two arms. Generally, L_A and L_B are made to be as similar as possible, therefore we can replace them with $L = (L_A + L_B)/2$ in (1.37). We still consider the minimal differences between the two in (1.36), which can be rewritten⁶ as

$$E^{(x/y)}(t) = \mp \frac{1}{2} E_0 e^{-i\omega_L (t - 2L/c) \pm i\phi_0 + i\Delta\phi_{x/y}(t)},$$

where

$$\phi_0 = k_L (L_A - L_B), \quad (1.38)$$

is a phase parameter that the experimenter can adjust. The strategy to build a "null instrument", which records zero signal when the gravitational wave is not passing, by setting $L_A = L_B \rightarrow \phi_0 = 0$, turns out to be failing, since it makes the instrument

⁵Note that if $L_A = L_B = L$, and $\frac{\omega L}{c} \ll 1$, the difference between the two would be

$$t_0^{(y)} - t_0^{(x)} = \frac{2L}{c} h\left(t - \frac{L}{c}\right) \text{sinc}\left(\omega L/c\right) \approx \frac{2L}{c} h\left(t - \frac{L}{c}\right).$$

⁶By using $2L_{A/B} = 2L \pm (L_A - L_B)$.

insensitive to calibration uncertainties. At the same time, setting the instrument to a phase where the variation is maximum, as for $\phi_0 = \pi/4$, makes the instrument too sensible, so much that it will not be able to distinguish a signal from the laser power fluctuations. Therefore, depending on how this parameter is adjusted the instrument can be more or less sensible to signal variations, and the best value tends to be between these two extremes.

1.3.2 LISA

Ground-based detectors such as LIGO and Virgo have pioneered the technique we have just shown in the high-frequency band ($\gtrsim 10$ Hz). The purpose for future space-based interferometers like LISA is to extend it to the low-frequency regime, opening a new observational window on astrophysical and cosmological sources. Indeed, space-based detectors such as LISA will be sensitive to DWDs with periods of a few hours down to a few minutes. At the shortest periods, these binaries are in very tight orbits, with separations of only a few 10^4 – 10^5 km, comparable to Earth’s diameter. Between the binary systems, the interacting ones can have extremely short orbital periods ($\lesssim 10$ minutes) and are strong, nearly monochromatic gravitational wave sources over LISA’s lifetime. Detached systems with periods in the mHz range are also important, as they provide long-lived, stable signals that can serve as calibration sources or “verification binaries” for space-based detectors. Given their abundance and gravitational wave luminosity, binary white dwarfs are expected to be the most numerous class of resolvable sources for LISA, and their unresolved population will form a significant component of the low-frequency gravitational wave foreground.

Instrument description

Earth-based detectors are limited in sensitivity in the low frequencies by seismic noise, gravity gradients from local mass movements, etc. Basing new detectors allows to eliminate these sources of noise, allowing to explore a frequency regime which contains precious information on many interesting astrophysical sources, such as DWDs, extreme mass-ratio inspirals and massive black hole mergers. In LISA’s case, the arms are not going to be physical structures, but 2.5×10^6 km separations between three identical spacecrafts at the vertices of an equilateral triangle. Each one of the spacecraft will host two free-falling test masses, isolated from all non-gravitational interactions by a drag-free control system. The spacecrafts will trail by about 20° , with the triangular constellation inclined by 60° to the ecliptic plane, following the earth around the sun. With this configuration, it is possible to keep the long baseline stable, while having continuous source visibility, and a good localization (granted by the triangular shape).

Frequency

LISA’s frequency band roughly covers the low range $0.1 \text{ mHz} \lesssim f \lesssim 1 \text{ Hz}$ (compared to LIGO’s frequency of 10 Hz to 1000 Hz), corresponding to objects in much wider orbits and potentially much heavier than those that LIGO is searching for, opening up the detection realm to a wider range of gravitational wave sources. In this frequency range also reside most DWDs. In the low frequencies, the range is limited by the acceleration

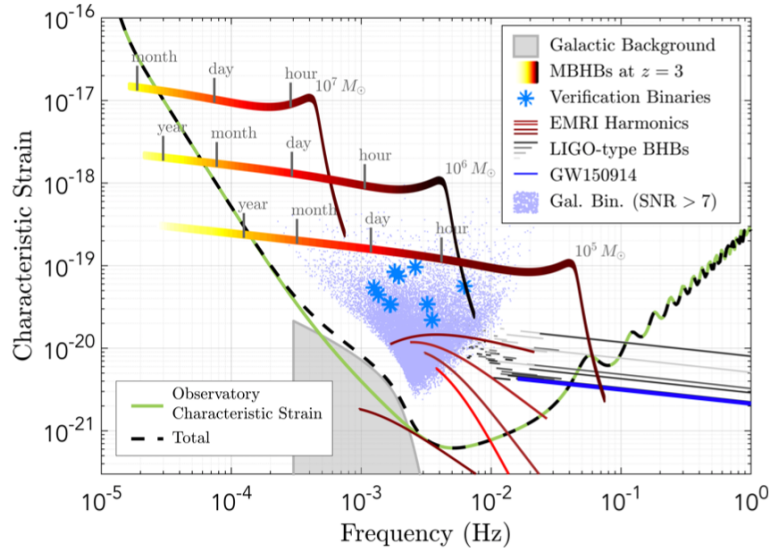


Figure 1.3: LISA sensitivity curve in the characteristic strain representation. The solid green line shows the instrumental noise curve, while the dashed black line represents the LISA curve as shaped by the background contribution from unresolved Galactic binaries. Different astrophysical sources that emit gravitational wave signal in this band are indicated: massive black hole binaries (MBHBs), extreme mass-ratio inspiral (EMRI), stellar-mass black hole binaries, verification binaries, and Galactic binaries with signal-to-noise ratio larger than 7. The source for this image is <https://ar5iv.labs.arxiv.org/html/1803.01944>

noise on the test masses: even in space, the "free" test masses are not completely isolated, but could be influenced by solar radiation and winds, and the "drag-free" micro-propellers that compensate these disturbances make noise under the $0.1mHz$. Also, in order to detect a very slow waves, LISA needs to observe it for at least one complete cycle, and if the wave has a period of months, the signal could become indistinguishable from a slow relative position change between the three satellites. At the high frequencies, the main limits are due to the arms length, which make LISA unable to detect waves much shorter than that scale, and the power limits of the laser, which makes the photon count Poissonian noise more relevant at high frequencies. LISA's sensitivity curve combines instrumental noise and the astrophysical foreground, including Galactic background and Galactic binary systems, as shown in **Figure 1.3**. As far as the frequency resolution of a coherent observation is concerned, the limits are not due to hardware, but the actual total observational time: in a Fourier analysis, this is set by the inverse of the total observation time:

$$\Delta f \approx \frac{1}{T_{\text{obs}}}. \quad (1.39)$$

For a nominal mission duration of $T_{\text{obs}} \simeq 4$ years, $\Delta f \approx 8 \times 10^{-9}$ Hz, allowing very fine separation of closely spaced monochromatic sources.

Why white dwarfs

As shown in Figure 1.3, we expect the Galactic binaries to generate a confusion foreground that is able to shape the LISA sensitivity curve, mostly due to their proximity and large number. The purpose of this work, however, is to discover if the extra-galactic binaries, despite their much greater distance, are sufficiently numerous to generate an overall detectable stochastic gravitational wave background in the LISA band. In particular, from a scientific perspective, DWDs offer a rich laboratory:

- The DWDs binary systems typically are in compact orbits, and the corresponding frequencies easily fall in LISA's band;
- The DWDs are some of the most common compact systems in the universe, that represent a probable output for binary system evolutions. When the number of non-resolvable sources is big, their signals superpose stochastically, generating a background;
- We have found a simple and predictable shape for their signal, in (1.32), which is easy to simulate, and allows to generate coherent synthetic populations with astrophysical models;
- As we said, we already expect galactic binaries to affect LISA's curve, therefore it is a natural realistic candidate to test;

The combination of abundance, signal strength, and astrophysical relevance makes them a target for LISA's mission that is worth exploring further.

Chapter 2

Methods and Data

The abundance of information of the electromagnetic spectrum allowed us to build highly detailed models of various celestial objects such as stars, both on their individual internal structure and on how this is influenced by the interaction with other bodies, for instance in binary systems. In the pursuit of reaching a greater sensitivity in the gravitational counterpart too, which could potentially reveal new information, or place better constraints on the existing models, these stellar models, when combined with a good theory of gravity, can be used to construct synthetic populations that reproduce observable features like luminosity, color, and chemical composition, which could enable us to predict what their gravitational signal would look like. In gravitational waves research, our observational capabilities are still very limited, and the signals are still comparatively very weak relative to their electromagnetic counterpart. Therefore, methods that rely on simulations can be very useful both to explore how different sources could look like in the gravitational wave domain, and how effectively they could be detected with current or future instruments.

2.1 Stellar Populations Synthesis Codes

Generating a synthetic population of stars is a very complex task, that involves multiple steps, each involving important choices. *First*, we need to choose a starting point: we could start from the very beginning of stars formation and simulate all the process from the birth onward, or we could select a later phase in the stars evolution, shared from the most, in order to reduce unnecessary computational power and time consumption. If we want to simulate entire stellar populations choosing a starting point also implies selecting appropriate distributions for the main parameters that characterize the "starting point population", like masses, metallicities, but also orbital parameters for the stars that are in binary systems, like orbital period, distance, and eccentricity. *Second*, we must choose how the stars will evolve from the starting point, and this involves the single star evolution but also the effects that interaction with other stars in binary systems have on it. *Finally*, we have to decide when we want to stop the simulation, choosing an endpoint that aligns with the needs of this study.

2.1.1 The starting point

As we know, in the Hertzsprung-Russell diagram, shown in **Figure 2.1**, which plots the *luminosity* of the stars in solar units vs their surface temperature in Kelvin, most of the stars appear distributed in the **main sequence (MS)**, a continuous and distinctive band. A star's position on this band is determined by its initial mass, and a good rule of thumb is that the most massive stars are hotter, more luminous, and evolve more quickly, while the lower-mass stars burn their fuel more slowly, and remain on the MS longer.

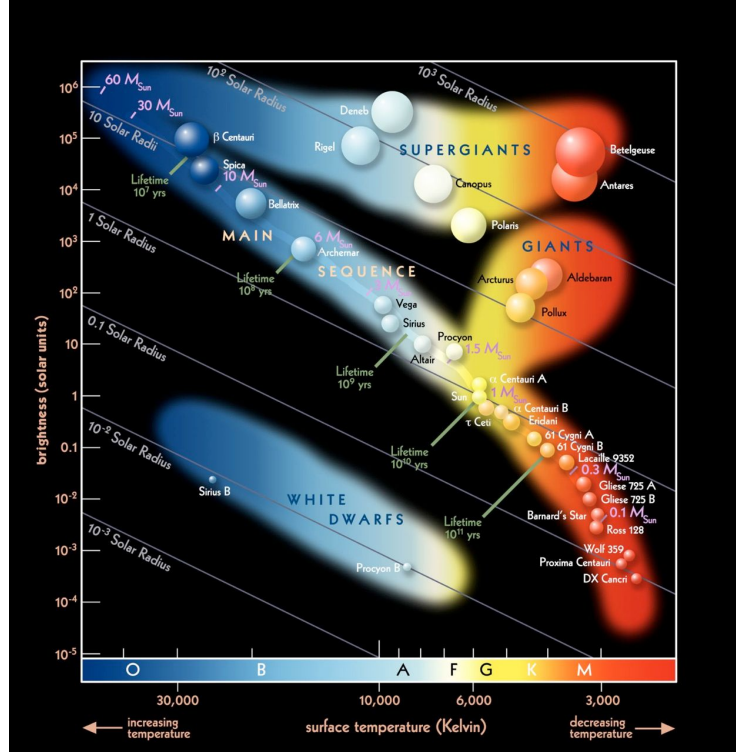


Figure 2.1: Hertzsprung–Russell (H–R) diagram showing the relationship between stellar luminosity (in solar units) and surface temperature (in Kelvin), that indicates the main stellar evolutionary stages: the main sequence, the giant and supergiant branches, and the white dwarf region. The source of the image is <https://asktheman.xyz/>

Since almost all stars go through a phase in the MS, and evolve from there differently, in this work, the chosen starting point for stellar evolution is the Zero Age Main Sequence (ZAMS). At this stage, stars have just begun hydrogen burning in their cores, marking the start of their stable main sequence phase. This allows to bypass the early phases of star formation, which are much less relevant to the gravitational wave sources of interest, while still capturing the essential evolutionary processes that lead to the formation of compact objects.

2.1.2 Single star evolution

Simulating the evolution of a single star is in itself a very complex matter, and the only way to make it computationally feasible in the context of large-scale population synthe-

sis is to approximate the evolution for a wide range of mass M and metallicity Z . In fact, detailed evolution codes can require substantial computational time even for the evolution of a single star, which is not practical when generating a full-scale astrophysical population containing millions of stars. Also, in order to make population synthesis statistically robust a large enough number of stars of a certain type must be evolved in order to overcome stochastic noise (in particular, the Poisson noise for n simulations of a particular type of star, implies an error that grows as \sqrt{n}). A winning strategy, adopted by several population synthesis frameworks, is to pre-generate a large grid of detailed stellar evolution models, and use them to derive a number of interpolation formulae as functions that approximate stellar properties as a function of age, mass and metallicity. In Hurley et al. [2000] this method is implemented through the development of a set of **Single Star Evolution (SSE)** formulae, with the result of a very compact, efficient and adaptable code, which makes it perfect for the integration of binary-star interactions. The work presented in Hurley et al. [2000] therefore serves as the theoretical and computational foundation for many complex stellar population synthesis codes, including the one used in this thesis. It takes care of the single-star evolution of stars from ZAMS through all the possible evolutionary outcomes, depending on the star's initial conditions.

2.1.3 Binary stars evolution

While the evolution of single stars already represents a challenge, the inclusion of binary interactions introduces a much higher level of complexity. In such systems, the evolution of each star is strongly influenced by its companion through a variety of processes, such as mass transfer and accretion, common envelope evolution, collisions, supernova kicks, tidal effects, angular momentum loss, and mergers. These interactions can drastically alter the final outcomes, and are essential for modeling the formation of compact binaries that are potential gravitational wave targets for LISA. To efficiently model binary evolution within the framework of stellar population synthesis, the work of Hurley et al. [2002] extends the SSE formalism by introducing a set of prescriptions for binary interactions, and updating the treatment of processes such as Roche lobe overflow, common envelope evolution and coalescence by collision, leading to the development of the **Binary Star Evolution (BSE)** algorithm. This code includes the interpolation-based approach used in SSE for single-star evolution, but adds a comprehensive treatment of binary-specific processes, enabling the simulation of a wide range of binary configurations but keeping the affordable computational requirements of SSE. The BSE algorithm tracks the joint evolution of both stars in a binary system, taking into account their initial parameters, such as masses, orbital period, eccentricity, and metallicity, and updates these properties dynamically as the system evolves. The flexibility and speed of the BSE code make it a key component in many modern population synthesis tools, including the one used in this thesis, which we will now introduce.

2.2 COSMIC

For the purposes of this work, we employ a community-developed binary population synthesis (BPS) python-based code, called the **Compact Object Synthesis and Monte**

Carlo Investigation Code (COSMIC), whose «*primary purpose is to generate synthetic populations with an adaptive size based on how the shape of binary parameter distributions change as the number of simulated binaries increases*»¹. COSMIC's binary evolution is built upon BSE, incorporating extensive modifications in order to include updated physical prescriptions. It includes all necessary tools to generate a population, from the generation of initial conditions, to scaling the simulated systems to full-scale astrophysical populations. The code is presented in Breivik et al. [2020], where it is described in full detail and used, as a proof of concept, to simulate the Galactic population of compact binaries and their associated gravitational wave signal. In the following section we will see the main features of the code, and explain what makes it the right choice for this thesis work.

2.2.1 Fixed population

A fundamental concept in COSMIC, which is the key to the code's efficiency, is the idea of *fixed population*. This refers to a relatively small sample² of just enough binaries to capture, in a statistically meaningful way, the underlying shape of the parameter distribution functions of the target population, as determined by the user specified Star Formation History (SFH) and evolution model. This is achieved following an iterative process designed to reach a convergence with respect to a defined matching condition, and consists of five key steps:

1. The user selects a binary evolution model and SFH;
2. Based on the SFH and the chosen initial parameter distribution, an initial population is generated;
3. The population evolves for a user specified number of steps, according to the selected evolution model;
4. If it is the first iteration, half of the simulated systems is compared with the total population. In the following steps, the population from the previous one gets compared to the population containing both the current and previous iterations. In any case, the comparison is done in order to check if the matching condition has been achieved;
5. Once the parameter distributions of the population have converged, the corresponding population is called *fixed population*, which represents the statistical features of a binary evolution model.

In practice, the fixed population is the converged, computationally efficient representation of the systems that we want to simulate, embedded in a complete small-scale synthetic galaxy that also contains other stellar components. The output is stored in a data frame, which separates the full galaxy properties from the fixed population ones. The last step required to construct a full size galaxy is to scale the fixed population (by mass

¹<https://cosmic-popsynth.github.io/docs/stable/pages/about.html>

²Note that, from now on, every time we talk about sampling, that is where the "M" of COSMIC comes into play: this code uses proficiently the Monte Carlo Markov Chain methods to sample populations and parameter distributions, as will follow in this section.

or by number of stars) with a re-sampling approach with replacement, allowing to extrapolate a larger final population that preserves the statistical properties encoded in the fixed population.

Initialization

The fixed population is generated from an initial collection of binaries sampled from distribution functions to assign to each binary an initial value of metallicity (Z), primary star mass (m), mass ratio (q), orbital separation (a), eccentricity (e), and birth time (T_0) according to the selected SFH. In COSMIC the user can choose between different binary parameter distributions, and different parameters can be treated independently. Moreover, COSMIC allows a complete personalization of the initial population through a number of other parameters, including different time-steps to control the binary physics, metallicity, stellar winds, common envelope phase, natal kicks, remnant mass, remnant spin, gravitational wave orbital decay, mass transfer, tides, and particular specifications for different kinds of stellar objects, mixing variables, and magnetic braking. In this work all the parameters were left default, but one: we tweaked the metallicity value, in order to differentiate fixed populations describing the parameter distributions for galaxies of different types. We will go more into detail on this topic in the next chapters.

Convergence

The number of simulated systems in the fixed population ideally describes the final parameter distribution functions while being low enough to keep the code efficient. Since every population depends on a different binary evolution model, to quantify this number a *discrete match criteria* is developed, based on the work Chatziioannou et al. [2017]. Independently generated histograms for each parameter are used to track their distribution as successive populations are generated and cumulatively added to the fixed population. The physical limits of the simulated systems are then enforced by taking the logistic transform, and finally the match is defined as:

$$match = \frac{\sum_{k=1}^N P_{k,i} P_{k,i+1}}{\sqrt{\sum_{k=1}^N (P_{k,i} P_{k,i}) \sum_{k=1}^N (P_{k,i} P_{k,i+1})}}, u$$

where $P_{k,i}$ is the probability for the k th bin, for the i th iteration. For how it is defined, the match value shifts between 0 and 1, and tends to unity as the parameter distributions converge to a distinct shape.

The output

Since COSMIC uses BSE as its core binary evolution algorithm, the output of COSMIC follows most of the same conventions as BSE. The *kstar values* (e.g. the number that represent a specific stellar type) and evolution stages are nearly identical to their BSE counterparts, and the exact references can be found in the **Appendix**. In order to generate a fixed population, the COSMIC can be ran through a one-line command directly on the terminal, specifying a parameter file, the kstar values for the primary and secondary star, the maximum number of systems to evolve, every how many systems to

check in, in order to track the distributions of the parameters, and how many processors to use. The final output is in an *hdf5* file containing several data frames, that keep track of various important quantities during the evolution: the total number of stars and total mass of the entire population, the number of binaries, the convergence, and so on. The *conv* data frame contains all the information about the final fixed population, and thus is the one that we will use the most: from it we can extract all the parameter distributions of the fixed population, such as the orbital parameters, and the individual star information. The parameter distributions of a fixed population of binary white dwarfs with a default metallicity value set at 0.020 is shown in Figure 2.2.

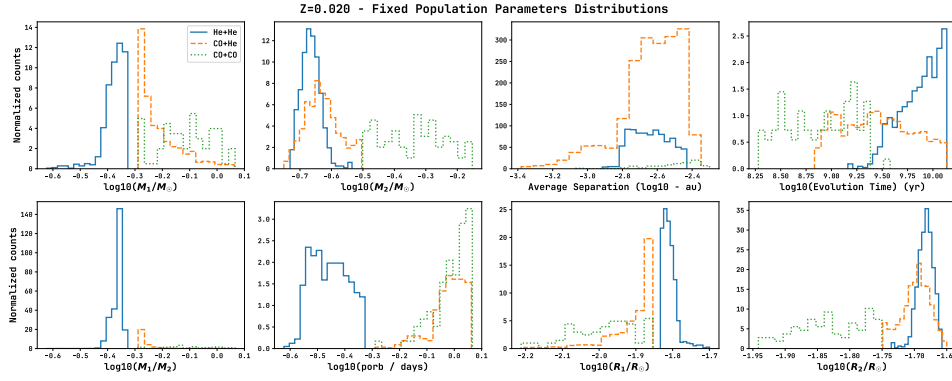


Figure 2.2: Distributions of the parameters of a fixed population with metallicity $Z = 0.020$ composed of He+He, CO+He and CO+CO binary white dwarfs. This includes the mass, radius of primary and secondary stars, the radius ratios between the two, the orbital period, average separation, and evolution time.

2.2.2 Astrophysical population

Once the convergence criteria is achieved, an astrophysical population can be sampled. The number of sources in the astrophysical population $N_{astro,tot}$ can be found by upscaling the size of the fixed population, N_{fixed} , by the ratio of the mass of the astrophysical population, M_{astro} , to the mass of all the stars in the whole small-scale galaxy in which the fixed population is embedded, $M_{fixed,stars}$, as follows:

$$N_{astro} = N_{fixed} \frac{M_{astro,tot}}{M_{fixed,stars}}, \quad (2.1)$$

or by the ratio of the number of stars in the astrophysical population, $N_{astro,tot}$, to the total number of stars formed to produce the fixed population, $N_{fixed,tot}$,

$$N_{astro} = N_{fixed} \frac{N_{astro,tot}}{N_{fixed,tot}}. \quad (2.2)$$

Thus, to create a full-scale astrophysical population we need a *reference population* from which we can extract either the total mass or the total number of stars, to then use to scale up our fixed population. As we will now see, the chosen reference for our purpose is a catalog which reports many key galactic parameters in it, which will allow us to proceed using the method in (2.1).

2.3 GWGC and Galaxy Properties

As we have seen, the goal of this work is to simulate the gravitational wave background produced by compact binaries in the *local universe*, by generating the sources using COSMIC. To replicate the existing, observed galaxies in the vicinity of the Milky Way and simulate their stellar content we rely on the dataset provided in White et al. [2011], the **Gravitational Wave Galaxy Catalog (GWGC)**. This catalog includes a list of 53,255 galaxies within $100Mpc$ from earth, containing information on sky position, distance, blue magnitude, major and minor diameters, position angle, and galaxy type, currently used for follow-up searches of electromagnetic counterparts from gravitational wave searches.

2.3.1 What it has vs what we need

In principle, we could generate a separate fixed population for each galaxy in the GWGC and scale it individually. However, this is simply not practical because of the computational power and time it would require, and therefore we must find a strategy to group them in a few, representative, categories. As we will show in this section, many of the information in the GWGC can be used to infer the missing astrophysical quantities we need for population synthesis. Ultimately, we will find that metallicity is the most suitable parameter for grouping galaxies. To get there, we follow a chain of empirical relations, starting from the galaxy morphological type, through a luminosity to mass, and then a mass to metallicity relation. This process will enable us to provide COSMIC with the necessary input, found in a consistent and astrophysically motivated way.

2.3.2 Mass-luminosity relation

As previously discussed, in order to scale a fixed population to the size of a specific galaxy, we need either its total stellar mass or the number of stars. In particular, Faber and Gallagher [1979] presents a luminosity-to-mass relation that depends on the morphological type. This allows to use the blue magnitude and the T-type provided in GWGC to estimate each galaxy's stellar mass.

Magnitude to luminosity

To compute the stellar mass, the luminosity-to-mass ratio presented in Faber and Gallagher [1979] applies to the absolute blue luminosity of each galaxy. GWGC provides the absolute blue magnitude, thus we have to convert it into blue luminosity using the Sun's blue-band absolute magnitude as a reference (typically $M_{B,\odot} = 5.48$). Starting from the magnitude definition,

$$m_{B,gal} - m_{B,\odot} = -2.5 \log_{10} \left(\frac{L_{B,gal}}{L_{B,\odot}} \right),$$

which, in stellar units, brings us to the following conversion:

$$L_{B,gal} = 10^{-0.4(m_{B,gal} - m_{B,\odot})} L_{B,\odot} \quad (2.3)$$

where $m_{B,gal}$ and $m_{B,\odot} \approx 5.48$ are the absolute blue magnitudes of the specific galaxy and the sun.

Galaxy morphological types

Although the GWGC denotes galaxy morphology using the de Vaucouleurs T-type scale, the luminosity-to-mass relations used in Faber and Gallagher [1979] are defined in terms of Hubble morphological classes. This classification is crucial because different morphological types exhibit significantly different stellar populations and star formation histories, which affect both luminosity and mass content. For example, elliptical galaxies generally have lower luminosity-to-mass ratios than spirals due to their older stellar populations and lack of ongoing star formation. Fortunately, a direct correspondence exists between T-type values and Hubble types, and thanks to the results in Faber and Gallagher [1979] we find the following correspondences:

T-Value	Hubble Class	$\frac{M}{L_B}$
−6.00 to −4.01	<i>E</i>	8.5
−4.00 to −2.01	<i>SO</i> [−]	9.5
−2.00 to −0.99	<i>SO</i> ⁺ − <i>S</i> _a	6.2
1.00 to 3.99	<i>S</i> _{ab} − <i>S</i> _{bc}	6.5
4.00 to 4.99	<i>S</i> _{bc} − <i>S</i> _c	4.7
5.00 to 5.99	<i>S</i> _{cd} − <i>S</i> _d	3.9
6.00 to 10.00	<i>S</i> _{dm} − <i>Irr</i>	8.5

Table 2.1: The first two columns of this table present a conversion between the Hubble class and the T-value classifications for the different galactic morphological types. This was done using the conversion table presented in https://en.wikipedia.org/wiki/Galaxy_morphological_classification. The last column associates at each galaxy type a mass-to-luminosity ratio, found using the work in Faber and Gallagher [1979].

The luminosity resulting from (2.3), expressed in units of solar blue luminosity $L_{B,\odot}$, can then be multiplied by the appropriate M/L_B ratio, as in Table 2.1, to yield the total stellar mass for the galaxy

$$M_{gal} = \frac{M}{L_B} L_{B,gal} \quad (2.4)$$

2.3.3 Mass-metallicity relation

Now that we have estimated the stellar mass of each galaxy, we can also derive the corresponding metallicity. This is made possible by the results of Tremonti et al. [2004], where an empirical relation between stellar mass and gas-phase oxygen abundance (a proxy for galaxy metallicity) is established. The study, based on a sample of over 50,000 star-forming galaxies observed by the Sloan Digital Sky Survey, reveals a tight correlation between stellar mass and metallicity, spanning three orders of magnitude in mass and a factor of ten in metallicity, which can be written as follows:

$$Z' = -1.492 + 1.847 \times \log(M_*) - 0.08026 \times [\log(M_*)]^2, \quad (2.5)$$

where M_* is the galactic stellar mass, and

$$Z' = 12 + \log(O/H) \quad (2.6)$$

is the metallicity written in terms of the oxygen abundance (all the metallicity values with an apostrophe are intended as in these units).

On metallicity units

Now, in these units the sun's metallicity is³ $Z'_{\odot} = 8.69$, whereas in the units used by COSMIC it is⁴ $Z_{\odot} = 0.0134$ (all the metallicity values without the apostrophe are intended as in these units). We can easily find a conversion between the two unit systems by assuming that the rate of oxygen abundance in the galaxy and the one in the sun is equal to the rate of the metallicities in COSMIC's units,

$$\frac{(O/H)_{gal}}{(O/H)_{\odot}} = \frac{Z_{gal}}{Z_{\odot}}, \quad (2.7)$$

where (O/H) can be found inverting (2.6). At this point, knowing that $Z'_{\odot} = 8.69$, we can:

- Compute the Z'_{gal} value for each galaxy in GWGC using (2.5);
- Write $(O/H)_{\odot}$ and $(O/H)_{gal}$ in terms of the corresponding Z' value using (2.6): $(O/H) = 10^{(Z'-12)}$ and $(O/H)_{\odot} \approx 0.32$.

Finally, finding Z_{gal} from (2.7), we can write the metallicity units conversion as:

$$Z_{gal} = 27.3 \times 10^{(Z'-12)}, \quad (2.8)$$

where the "27.3" coefficient mainly depends on the Z_{\odot} value. This relation allows us to assign a realistic metallicity estimate to each GWGC galaxy in COSMIC's units, which we can now use to group them into representative subsets. This way, we can account for the significant impact of metallicity on stellar wind strength, remnant masses, and binary evolution outcomes, that greatly affects the expected gravitational wave signal.

2.3.4 Missing galaxies

The GWGC is far from being a complete list of the galaxies in the local Universe. As we will now see, there are two main factors contributing to this incompleteness: observational limitations due to the Zone of Avoidance (ZOA) and limitations of the information that the catalog presents.

Zone of avoidance

Since the GWGC is an observation-based catalog compiled from optical surveys, we must account for the Zone of Avoidance — the region of the sky obscured by the Milky Way's interstellar dust and stellar crowding, which impedes the detection of background galaxies. The extent of the ZOA depends on the wavelength of observation: infrared surveys penetrate deeper through the dust, while optical surveys, like those used for GWGC, are more strongly affected. In the optical band, the ZOA is expected to cover

³This value is taken from the work Allende Prieto et al. [2001]

⁴This refers to the work Asplund et al. [2009]

about $\sim 25\%$ of the sky Kraan-Korteweg and Lahav [2000]. For this work, we estimated the ZOA directly from the spatial distribution of galaxies in GWGC, by plotting their positions in Galactic coordinates. This way, the ZOA appears clearly as a horizontal band centered around the Galactic plane (see Figure 2.3). To quantify its extent, we used a Python package that handles pixelated data on the sphere based on the Hierarchical Equal Area isoLatitude Pixelization (HEALPix, <https://sourceforge.net/projects/healpix/>), called healpy, to divide the sky map into n_{pix} equal-area pixels, and focused on the band $|b| \leq 15^\circ$ in Galactic latitude. Counting the empty pixels in this band and dividing by n_{pix} gives an estimated ZOA coverage of $\sim 20\%$ – 25% of the sky, depending on the chosen pixel resolution. This estimate is fully consistent with the literature Kraan-Korteweg and Lahav [2000], so in our analysis we will assume that GWGC effectively covers $\sim 80\%$ of the sky.

Incompleteness and non-galactic objects

Secondly, the entries of the GWGC represent a source of incompleteness themselves. Not all the objects listed in the GWGC are suitable for our purposes: in addition to galaxies, the catalog also includes globular clusters, which can be identified through their T-type values; moreover, not all galaxies in the catalog contain all the information required to perform the procedures described in the previous sections. To construct a working sample, we applied a series of masks to clean the catalog:

- Only keep entries classified as galaxies;
- Require that the distance, T-type, and absolute blue magnitude are provided;

After this selection, the sample we are left with scaled down in size, from the original 53,255 entries to 20,246 galaxies suitable for population synthesis.

Filling the gap

In order to compensate the missing galaxies, we have made two physically motivated assumptions.

1. Cosmological Principle:

The GWGC lists all the observed galaxies within $100Mpc$. On such scales, the Universe can be assumed to be statistically *homogeneous* and *isotropic*. This assumption is supported from observations of the *Cosmic Microwave Background* (CMB), where we know that the correlation function of the temperature fluctuations across the sky peaks at scales of $\sim 100Mpc$. Under this assumption, the selected galaxies of the GWGC should be statistically representative of the overall population in the same volume.

2. Distance Matters:

The angular position is irrelevant in the computation of the gravitational wave signal; only the distance of the source matters. Therefore, missing galaxies from the unexplored volume covered by the Milky Way can be statistically represented by the galaxies from our retained sample.

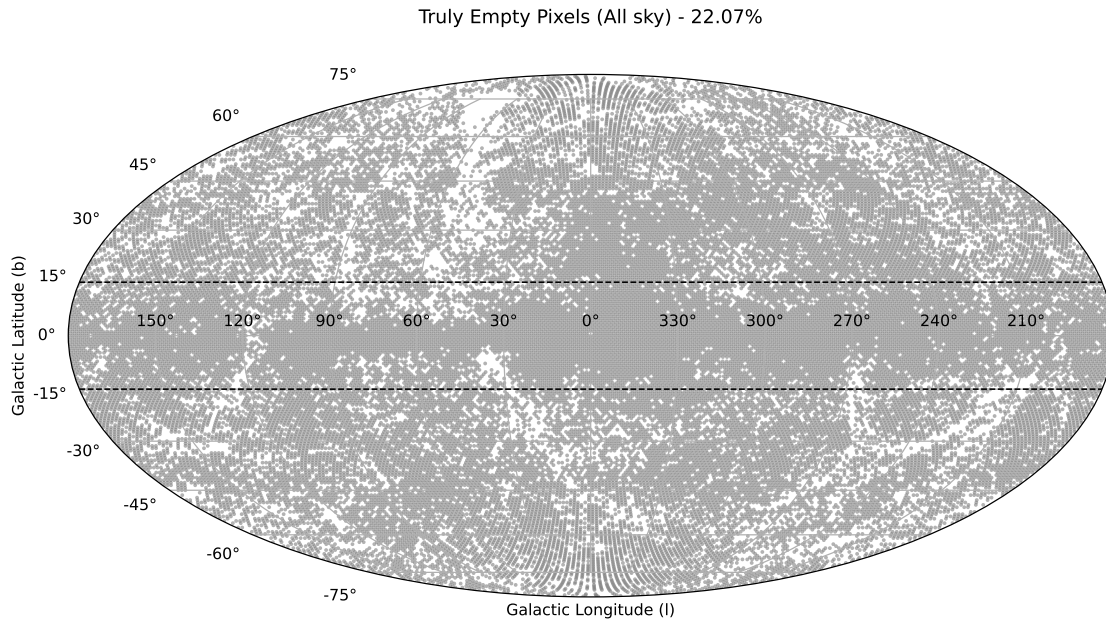


Figure 2.3: Visual representation of the regions of the sky not covered by any of the 53,255 galaxies in the GWGC, plotted in galactic coordinates using `healpy`, a Python package that handles pixelated data on the sphere based on the Hierarchical Equal Area isoLatitude Pixelization (**HEALPix**, <https://sourceforge.net/projects/healpix/>). This library allows the user to choose the number of pixels, and thus their size, through a power-of-2 parameter in the `nside2npix` function: the larger the parameter, the smaller the pixel and the bigger their number. The gray dots in the figure represent the empty sky pixels, while the white areas correspond to pixels containing at least one galaxy. The central band, where the Milky Way lies, appears significantly emptier than the rest of the sky; this is the so called Zone Of Avoidance (ZOA). To estimate the ZOA, we calculated the percentage of empty pixels in the band $|b| \leq 15^\circ$ in Galactic latitude. Choosing the parameter to be too small, the produced pixels would be too large, and the empty area would be underestimated. Larger values would make the estimation only more precise, and by selecting parameters starting from $2^6 = 64$, it's possible to estimate roughly $\sim 20\%$ – 25% of empty sky, fully consistent with the value reported in Kraan-Korteweg and Lahav [2000]. The 22.07% estimation in the title is found using 64 as parameter value.

Following these assumptions, we “fill in” the missing fraction of the sky and the dropped entries of the catalog by sampling with replacement from the cleaned GWGC, just like we did to extract an astrophysical from the fixed one, preserving its parameter distributions. This ensures that the statistical properties of the synthetic galaxy distribution match those of the observed portion while restoring the full-sky coverage. This is shown in a graphical representation of the distributions of distances, blue band magnitudes and T-types, in **Figure 2.4**: the distributions have been scaled up without visible changes.

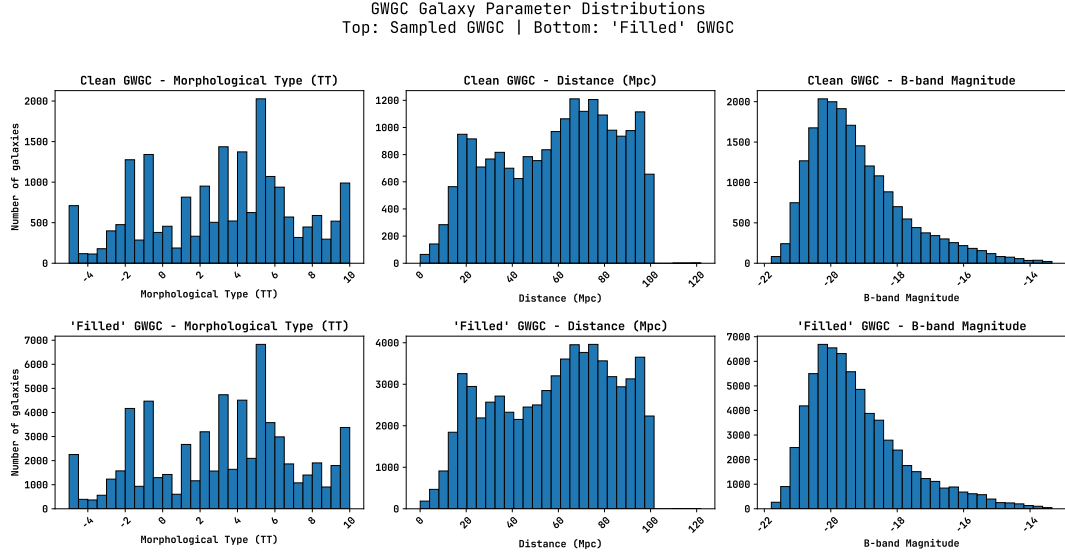


Figure 2.4: Distributions of T-value, distance and B-band magnitude of the galaxies in the Gravitational Wave Galaxy Catalog (GWGC) before and after compensating for the lack of galaxies due to the catalog’s incompleteness and the **Zone Of Avoidance (ZOA)**. The three graphs *above* show the mentioned distributions for the 20,246 galaxies of the original GWGC after we dropped those missing the key parameters we needed; the three graphs *below* show the same distributions for the 66,568 galaxies we are left with after taking into account both the catalog’s incompleteness and the ZOA with a sampling with replacement method. The parameters distributions appear to be indistinguishable in shape: the scaling up in size left the properties of the catalog.

The total number of galaxies that we have, now that we took into consideration both the dropped galaxies of the original GWGC and the ones covered by the ZOA, is 66,568.

2.4 Final Steps

Now that the catalog has been completed and its ready for the population synthesis, its time to put all the pieces together. We will analyze the metallicity distribution of the galaxies in the final catalog, categorize and generate the fixed populations accordingly, and make some final considerations regarding LISA’s frequency resolution, how to take care of it, and how to sum gravitational wave signals of multiple sources that LISA will not be able to distinguish.

2.4.1 The final fixed populations

As we already discussed, the metallicity of a galaxy has a great impact on the stellar evolution and, thus, gravitational wave signal. This, plus the fact that metallicity is closely linked to the galaxy types too, led us to choose it as characterizing parameter for the populations that we will generate to represent the galaxy in the catalog. In particular, the final catalog covers a range from a minimum of $Z = 0.00748$ to a maximum of $Z = 0.03948$. We decided to group all the values in between in ten equally wide bins, represented in Figure 2.5.

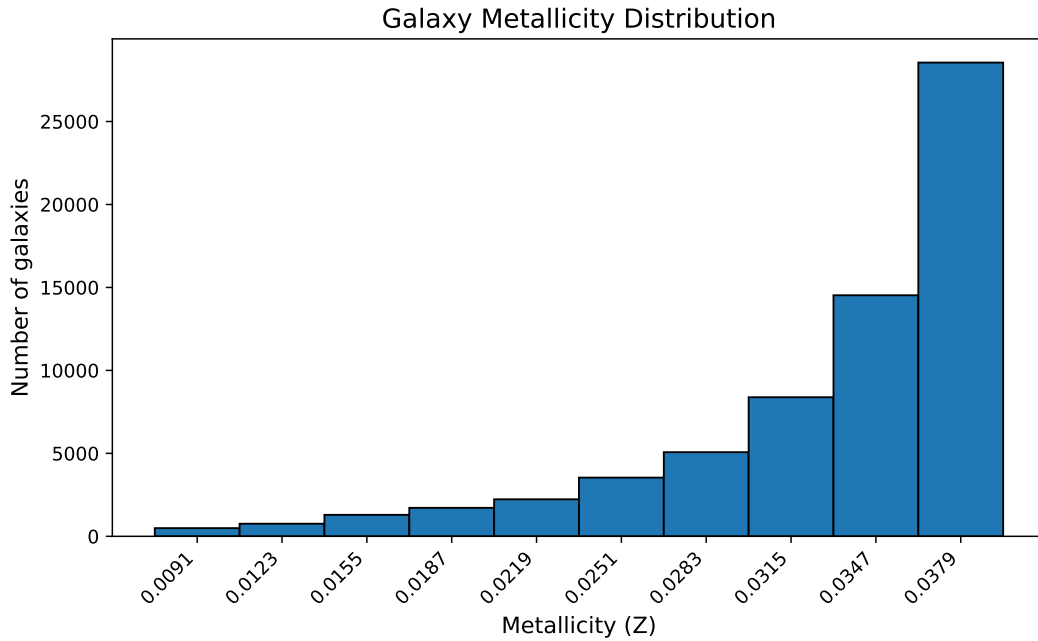


Figure 2.5: Metallicity distribution of the final galaxy catalog. The metallicity of the galaxies has been shown to correlate with their morphological type Faber and Gallagher [1979]. Therefore, the entries of our final catalog can be grouped into 10 bins, each associated to a metallicity value (the middle value of the corresponding bin, shown in the x -axis label of the graph), and a corresponding fixed population.

Each one of the center values of the bins, shown in the x label, is linked to a different synthetic fixed population generated with COSMIC. The simulation was done generating the fixed populations "*the cosmic way*", via terminal, specifying $Nstep = 5000$ and $Niter = 1000000000$ and $kstar$ values 10, 11 and 12, corresponding to He, CO, and Ne white dwarfs⁵.

2.4.2 LISA's frequency resolution

The duration of LISA's mission directly impacts its frequency resolution: the longer the observation time, the finer the frequency bins it can resolve. In this work, we assume

⁵All the $kstar$ values and the corresponding astrophysical objects are shown in Table A.1, in the Appendix.

an observation time of:

$$T_{obs} = 4yr = 126,144,000s$$

which corresponds to a minimum frequency resolution of

$$\delta\nu_{LISA,min} \approx \frac{1}{T_{obs}} \sim 8 \times 10^{-9} Hz. \quad (2.9)$$

This fundamental limit comes from the Fourier transform properties, and determines the smallest frequency interval over which the signals can be resolved. Although this is a very fine resolution, the precision of the orbital period in the simulated binary systems, and thus the frequency resolution on their gravitational signal, is actually much bigger, since these values come from a simulation rather than from real observations. For this reason, when computing the gravitational wave signals of our simulated binaries, we must take into account the fact that LISA will not be able to distinguish sources whose sources fall in the same frequency bin. To model this, we group the resulting gravitational wave signals in bins of size $\delta\nu_{LISA,min}$, and sum all the signals that fall within each bin, as we will now explain.

Multiple signals summation

To accurately represent the frequency resolution limit imposed by LISA's observation time, we have to sum all the signals within the same frequency bin. In principle, over the observation time T_{obs} , the orbital parameters of the sources may slowly evolve, causing a drift in the gravitational wave frequency. Integrating the resulting signal during this period is no easy task. However, for the slowly evolving white dwarf binaries we are considering, the change in such short time-frames is negligible, so we can treat their signals as effectively monochromatic within the observation window. Thus, we can define a commonly used variable to simplify our job, which is called **Amplitude Spectral Density (ASD)**:

$$ASD = h\sqrt{T_{obs}}, \quad (2.10)$$

where h is the gravitational wave strain of the binary, computed in (1.32), and T_{obs} is the mission duration for LISA. This quantity represents the characteristic strain amplitude of the gravitational wave signal per square root of frequency, scaled by the observation time, and its very convenient for comparing the signals in frequency space. Correspondingly, we can define the **Power Spectral Density (PSD)** as the square of the ASD

$$PSD = ASD^2, \quad (2.11)$$

which properly represents the signal power per frequency unit. Since power contributions from independent sources add linearly, the total PSD in a given frequency bin is simply found by summing the power of all the sources within it:

$$PSD_{tot,bin_1} = PSD_{1,bin_1} + PSD_{2,bin_1} + \dots \quad (2.12)$$

This way, we effectively accounted for LISA's frequency resolution limit. The reason for introducing this quantities is that gravitational waves from different binaries are uncorrelated, so their strains add incoherently. This means we cannot simply sum the strain amplitudes directly. Instead, the PSD provides a way to combine signals that ensures a correct representation of the combined gravitational wave background.

Chapter 3

Results and Discussion

Up to this point, we have laid the theoretical and methodological foundations of our investigation: from the gravitational wave theory, to the astrophysical context of white dwarfs and their host galaxies, the principles of gravitational wave detection, and finally the construction of the simulated populations used in this work. In this chapter, we finally turn to the quantitative results on the generation of the corresponding gravitational wave signal. We begin by applying the computational pipeline described in the previous chapter to our final galaxy catalog, extracting the gravitational wave signal from the simulated populations of binary white dwarfs. The resulting spectra are then compared to the LISA sensitivity curve to verify the detectability of an extragalactic background. We then discuss the frequency distribution and amplitude characteristics of the simulated signals, as well as the physical reasons underlying our results, and their implications for future space-based gravitational wave detectors.

3.1 The Signal Computation

In order to compute the total extragalactic DWDs gravitational background, we must apply an iterative process to each galaxy in the final catalog, which consists of the following steps:

- Compute the right N_{astro} using the (2.1)
- Scale the fixed population accordingly with a sampling with replacement method, creating the full-size galaxy simulation.

At this point for each binary system in this astrophysical population we:

- Compute the gravitational wave signal using (1.32)¹ and the corresponding PSD using (2.10) and (2.11);
- Sum the total PSD of the binaries whose frequencies fall within the same LISA's frequency bin, using (2.12);
- Plot the total binned signals on LISA's curve.

¹Note here that all the binaries within the same galaxy are given the same distance from us. This approximation is considered to be valid since the distance of the galaxy is much much bigger than its size, and thus the maximum possible distance between two binaries within the same galaxy.

LISA's sensitivity curve

The LISA curve is constantly updated when new gravitational wave components that can affect it are found, meaning that there are many different versions around. The one we chose to use is the widely used version made by Robson et al. [2019], which is written as:

$$S_n = \frac{10}{3L^2} \left(P_{OMS}(f) + \frac{4P_{acc}(f)}{(2\pi f)^4} \right) \left(1 + \frac{6}{10} \left(\frac{f}{f_*} \right)^2 \right) + S_c(f), \quad (3.1)$$

where $L = 2.5Gm$ is the LISA arm length, $f_* = 19.09mHz$ and $P_{OMS}(f)$, $P_{acc}(f)$ and $S_c(f)$ are the expressions for the single-link optical metrology noise, the single test mass acceleration noise and the total Michaelson-style LISA data channel. The equations for these factors, as well as more detail on the curve that we chose, can be found in the article. Doing this, the spectral distribution of the final resulting signal is plotted over the LISA's sensitivity curve² in Figure 3.1 Every orange dot in Figure 3.1 represents

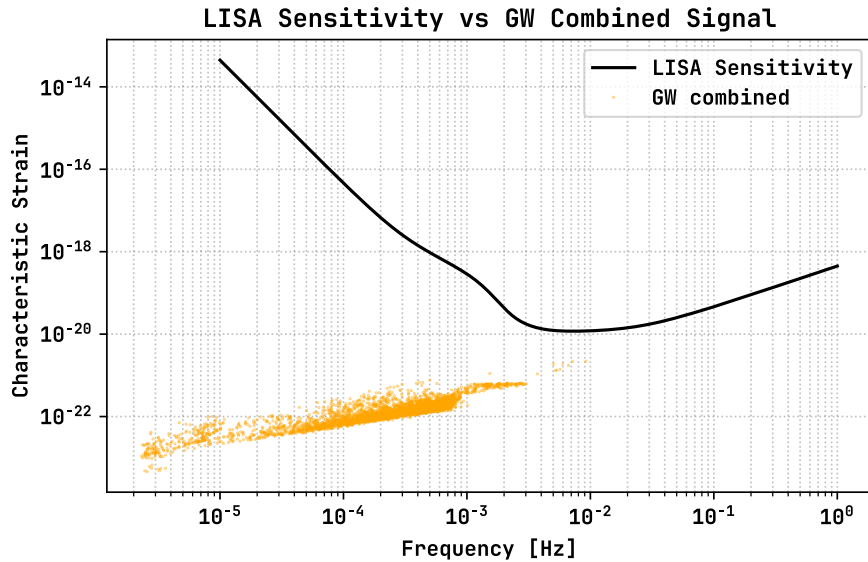


Figure 3.1: Total gravitational wave signal of the simulated Double White Dwarfs (DWDs) hosted by the 66,568 galaxies of the final catalog, binned in $\sim 8 \times 10^{-9}Hz$ large frequency bins, representing LISA's spectral resolution. Every orange dot represents the signal of a frequency bin, calculated by summing the Power Spectral Density (PSD) of every galaxy that it contained, using (2.12). The dots are plotted on LISA's sensitivity curve, as found in Robson et al. [2019], and appear to be about one order of magnitude below the minimum threshold of this curve. This results suggest that we should not expect LISA to be able to detect the unresolved extragalactic DWDs confusion foreground, at least under the assumptions and approximations adopted in this work.

a frequency bin, whose width is given by (2.9), where the signal of a certain number of simulated binaries has been summed using (2.12). As we can see, the resulting signal

²This particular curve is presented in Robson et al. [2019].

appears to be about one order of magnitude smaller than the minimum detectable strain for LISA across the whole band. This indicates that the stochastic contribution from extragalactic DWDs will not have a measurable impact on LISA's sensitivity curve, at least under the assumptions of our population model and scaling relations.

Distribution of the sources. The simulated extragalactic binaries populate primarily the low-frequency range ($f \lesssim 2$ mHz), with the number of systems decreasing steeply at higher frequencies. Because of the nature of binary formation, at higher frequencies the binary system have had enough time to evolve, and have thus a broader range of orbital frequencies where to spread. Once they get high enough in the spectrum, the faster orbital decay of short-period binaries causes the absence of gravitational wave signals at higher frequencies. Moreover, the spectral shape of the resulting background is positioned at frequencies that are similar to the expected Galactic foreground ones (corresponding to the slight bump at the left of the lowest point in the graph - this is better shown in Figure 1.3), but with a significantly lower amplitude due to the much larger average distances. Indeed, as shown in (1.32), the gravitational wave amplitude scales inversely with the distance from the source, so even relatively nearby galaxies contribute far less per binary than the Milky Way population. The total number of galaxies in the local Universe, even if large, is not sufficient to compensate for this distance-induced amplitude suppression in the LISA band.

Conclusions and Future Perspectives

In this thesis we investigated the contribution of extragalactic double white dwarf (DWD) binaries to the low-frequency gravitational wave (GW) background, with a focus on their potential detectability by the space-based interferometer LISA. We began by discussing the theoretical gravitational wave framework, and the astrophysical elements that are relevant to this problem, including a brief description of the formation and evolution of white dwarfs, both as isolated stars and in binary systems, and the galactic environments in which they reside and evolve. We then discussed the fundamentals of interferometric detection, and the specific capabilities of LISA as a space-based detector. On this theoretical basis, we developed a computational pipeline to simulate synthetic populations of extragalactic DWD binaries using the population synthesis code COSMIC. We then scaled them according to the stellar masses of host galaxies, using the astrophysical observations galaxy survey "*Gravitational Wave Galaxy Catalog*" as reference, and computed their GW strain and power spectral density. The simulated signals were finally binned according to LISA's frequency resolution and compared with its sensitivity curve. The main result of this study is that the predicted gravitational wave signal from the extragalactic DWD population lies approximately one order of magnitude below LISA's detection threshold, as found in Robson et al. [2019], across the considered frequency band. Therefore, although, as we know, DWD binaries are expected to constitute a dominant foreground from Galactic sources, able to shape LISA's curve substantially, the extragalactic component is not expected to measurably affect it at all. While the present analysis points towards a negligible extragalactic contribution for LISA, it provides a quantitative baseline that can be refined in several directions. For example, future work could incorporate more detailed galaxy catalogs with redshift-dependent star formation histories and metallicity evolution, and that take in account more precisely the missing sources blocked from our Galaxy in the *Zone Of Avoidance*. Similarly, improving the binary population synthesis models, for example by including different prescriptions also on other parameters, and not only focusing on the metallicity, like mass transfer prescriptions or alternative common-envelope outcomes. Moreover, since population synthesis is a very active and rapidly evolving research field, testing alternative codes, possibly based on different Single Star and Binary Stars evolution models, could help quantify the model dependence of our predictions and reveal systematic uncertainties. Finally, although the extragalactic DWD background may be undetectable for LISA, this work shows how future space-based detectors with longer baselines or improved sensitivity in the sub-millihertz regime could, in principle, probe this population, offering a complementary view to Galactic studies and providing constraints on the binary evolution across cosmic time. In summary, this work has explored a previously the extragalactic DWDs component of the GW landscape, reinforcing the understanding that

the gravitational wave sky at low frequencies will be dominated by Galactic sources, but also highlighting that the extragalactic background, though faint, remains a scientifically interesting target for the next generation of detectors.

Appendix A

Table A.1: In this table are presented all the possible kstar values that the user can choose in COSMIC, and the corresponding astrophysical object.

kstar value	evolutionary state
0	Main Sequence (MS), $< 0.7M_{\odot}$
1	MS, $> 0.7M_{\odot}$
2	Hertzsprung Gap
3	First Giant Branch
4	Core Helium Burning
5	Early Asymptotic Giant Branch (AGB)
6	Thermally Pulsing AGB
7	Naked Helium Star MS
8	Naked Helium Star Hertzsprung Gap
9	Naked Helium Star Giant Branch
10	Helium White Dwarf
11	Carbon/Oxygen White Dwarf
12	Oxygen/Neon White Dwarf
13	Neutron Star
14	Black Hole
15	Massless Remnant

Appendix B

Dettagli tecnici sul codice.

Tabelle di parametri.

Ulteriori grafici.

Script di calcolo, se rilevante.

Bibliography

- Carlos Allende Prieto, David L. Lambert, and Martin Asplund. The Forbidden Abundance of Oxygen in the Sun. *ApJ*, 556(1):L63–L66, July 2001. doi: 10.1086/322874.
- Martin Asplund, Nicolas Grevesse, A. Jacques Sauval, and Pat Scott. The Chemical Composition of the Sun. *ARA&A*, 47(1):481–522, September 2009. doi: 10.1146/annurev.astro.46.060407.145222.
- Katelyn Breivik, Scott Coughlin, Michael Zevin, Carl L. Rodriguez, Kyle Kremer, Claire S. Ye, Jeff J. Andrews, Michael Kurkowski, Matthew C. Digman, Shane L. Larson, and Frederic A. Rasio. COSMIC Variance in Binary Population Synthesis. *ApJ*, 898(1):71, July 2020. doi: 10.3847/1538-4357/ab9d85.
- Katerina Chatziioannou, James Alexander Clark, Andreas Bauswein, Margaret Millhouse, Tyson B. Littenberg, and Neil Cornish. Inferring the post-merger gravitational wave emission from binary neutron star coalescences. *Phys. Rev. D*, 96(12):124035, December 2017. doi: 10.1103/PhysRevD.96.124035.
- S. E. de Mink, O. R. Pols, and R. W. Hilditch. Efficiency of mass transfer in massive close binaries. Tests from double-lined eclipsing binaries in the SMC. *A&A*, 467(3): 1181–1196, June 2007. doi: 10.1051/0004-6361:20067007.
- Gerard de Vaucouleurs, Antoinette de Vaucouleurs, Herold G. Corwin, Jr., Ronald J. Buta, Georges Paturel, and Pascal Fouque. *Third Reference Catalogue of Bright Galaxies*. 1991.
- Michal Dominik, Krzysztof Belczynski, Christopher Fryer, Daniel E. Holz, Emanuele Berti, Tomasz Bulik, Ilya Mandel, and Richard O’Shaughnessy. Double Compact Objects. I. The Significance of the Common Envelope on Merger Rates. *ApJ*, 759(1):52, November 2012. doi: 10.1088/0004-637X/759/1/52.
- Albert Einstein. Über Gravitationswellen. *Sitzungsberichte der Königlich Preussischen Akademie der Wissenschaften*, pages 154–167, January 1918.
- S. M. Faber and J. S. Gallagher. Masses and mass-to-light ratios of galaxies. *ARA&A*, 17:135–187, January 1979. doi: 10.1146/annurev.aa.17.090179.001031.
- V. Ferrari, L. Gualtieri, and P. Pani. *General Relativity and its Applications: Black Holes, Compact Stars and Gravitational Waves*. CRC Press, 1st edition, 2020. doi: 10.1201/9780429491405. URL <https://doi.org/10.1201/9780429491405>.

- Aaron M. Geller, Nathan W. C. Leigh, Mirek Giersz, Kyle Kremer, and Frederic A. Rasio. In Search of the Thermal Eccentricity Distribution. *ApJ*, 872(2):165, February 2019. doi: 10.3847/1538-4357/ab0214.
- D. Goldberg and T. Mazeh. The mass-ratio distribution of the spectroscopic binaries in the Pleiades. *A&A*, 282:801–803, February 1994.
- D. C. Heggie. Binary evolution in stellar dynamics. *MNRAS*, 173:729–787, December 1975. doi: 10.1093/mnras/173.3.729.
- E. P. Hubble. Extragalactic nebulae. *ApJ*, 64:321–369, December 1926. doi: 10.1086/143018.
- Jarrold R. Hurley, Onno R. Pols, and Christopher A. Tout. Comprehensive analytic formulae for stellar evolution as a function of mass and metallicity. *MNRAS*, 315(3): 543–569, July 2000. doi: 10.1046/j.1365-8711.2000.03426.x.
- Jarrold R. Hurley, Christopher A. Tout, and Onno R. Pols. Evolution of binary stars and the effect of tides on binary populations. *MNRAS*, 329(4):897–928, February 2002. doi: 10.1046/j.1365-8711.2002.05038.x.
- J. Klencki, M. Moe, W. Gladysz, M. Chruslinska, D. E. Holz, and K. Belczynski. Impact of inter-correlated initial binary parameters on double black hole and neutron star mergers. *A&A*, 619:A77, November 2018. doi: 10.1051/0004-6361/201833025.
- Renée C. Kraan-Korteweg and Ofer Lahav. The Universe behind the Milky Way. *A&A Rev.*, 10(3):211–261, January 2000. doi: 10.1007/s001590000011.
- Pavel Kroupa. On the variation of the initial mass function. *MNRAS*, 322(2):231–246, April 2001. doi: 10.1046/j.1365-8711.2001.04022.x.
- Pavel Kroupa, Christopher A. Tout, and Gerard Gilmore. The Distribution of Low-Mass Stars in the Galactic Disc. *MNRAS*, 262:545–587, June 1993. doi: 10.1093/mnras/262.3.545.
- Michele Maggiore. *Gravitational Waves: Volume 1: Theory and Experiments*. Oxford University Press, 10 2007. ISBN 9780198570745. doi: 10.1093/acprof:oso/9780198570745.001.0001. URL <https://doi.org/10.1093/acprof:oso/9780198570745.001.0001>.
- Tsevi Mazeh, Dorit Goldberg, Antoine Duquennoy, and Michel Mayor. On the Mass-Ratio Distribution of Spectroscopic Binaries with Solar-Type Primaries. *ApJ*, 401: 265, December 1992. doi: 10.1086/172058.
- Maxwell Moe and Rosanne Di Stefano. Mind Your Ps and Qs: The Interrelation between Period (P) and Mass-ratio (Q) Distributions of Binary Stars. *ApJS*, 230(2):15, June 2017. doi: 10.3847/1538-4365/aa6fb6.
- Travis Robson, Neil J Cornish, and Chang Liu. The construction and use of lisa sensitivity curves. *Classical and Quantum Gravity*, 36(10):105011, April 2019. ISSN 1361-6382. doi: 10.1088/1361-6382/ab1101. URL <http://dx.doi.org/10.1088/1361-6382/ab1101>.

- Edwin E. Salpeter. The Luminosity Function and Stellar Evolution. *ApJ*, 121:161, January 1955. doi: 10.1086/145971.
- Christy A. Tremonti, Timothy M. Heckman, Guinevere Kauffmann, Jarle Brinchmann, Stéphane Charlot, Simon D. M. White, Mark Seibert, Eric W. Peng, David J. Schlegel, Alan Uomoto, Masataka Fukugita, and Jon Brinkmann. The Origin of the Mass-Metallicity Relation: Insights from 53,000 Star-forming Galaxies in the Sloan Digital Sky Survey. *ApJ*, 613(2):898–913, October 2004. doi: 10.1086/423264.
- L. M. van Haaften, G. Nelemans, R. Voss, S. Toonen , S. F. Portegies Zwart, L. R. Yungelson, and M. V. van der Sluys. Population synthesis of ultracompact X-ray binaries in the Galactic bulge. *A&A*, 552:A69, April 2013. doi: 10.1051/0004-6361/201220552.
- Darren J White, E J Daw, and V S Dhillon. A list of galaxies for gravitational wave searches. *Classical and Quantum Gravity*, 28(8):085016, March 2011. ISSN 1361-6382. doi: 10.1088/0264-9381/28/8/085016. URL <http://dx.doi.org/10.1088/0264-9381/28/8/085016>.